Cell Systems

Article

Apparent simplicity and emergent robustness in the control of the *Escherichia coli* cell cycle

Graphical abstract

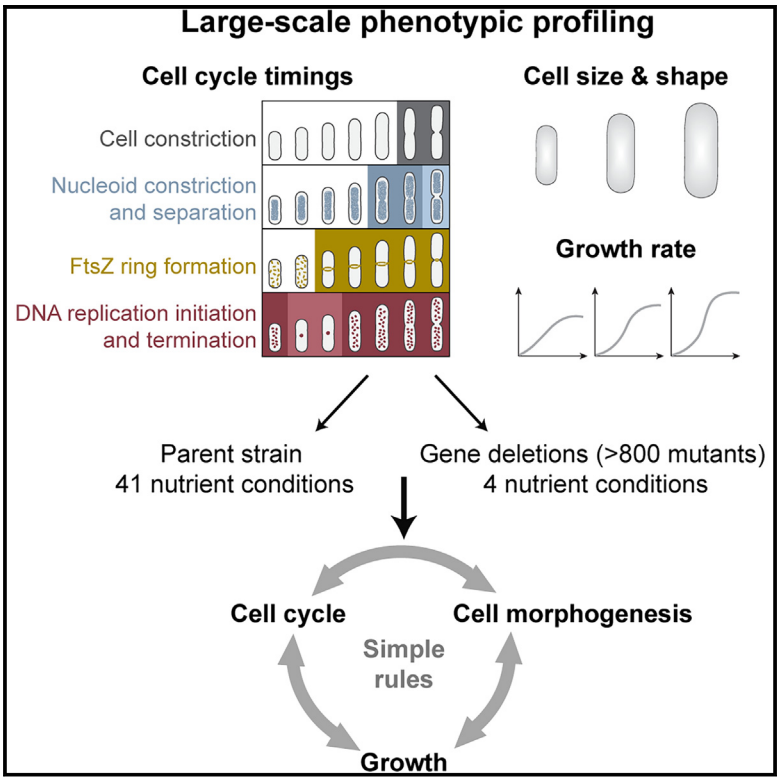

Highlights

- Large-scale phenotyping of *E. coli* cell morphology, cell cycle events, and growth
- Extensive phenotypic plasticity of gene deletions across nutrient conditions
- Emergence of 5 robust cell cycle laws across genetic and metabolic perturbations
- Population-level integration of cell cycle processes and growth rate with cell size

Authors

Sander K. Govers, Manuel Campos, Bhavyaa Tyagi, Géraldine Laloux, Christine Jacobs-Wagner

Correspondence

jacobs-wagner@stanford.edu

In brief

By characterizing morphological, cell cycle, and growth features across perturbations, Govers et al. identify simple governing principles of cell cycle control in *Escherichia coli*. These population-level principles connect cell cycle events to specific aspects of cell size, providing an average picture by which *E. coli* can achieve robust cell proliferation.

Govers et al., 2024, Cell Systems *15*, 19–36
January 17, 2024 © 2023 The Author(s). Published by Elsevier Inc.
https://doi.org/10.1016/j.cels.2023.12.001

CellPress

Cell Systems

CellPress
OPEN ACCESS

Article

Apparent simplicity and emergent robustness in the control of the *Escherichia coli* cell cycle

Sander K. Govers,[1,2,3] Manuel Campos,[4] Bhavyaa Tyagi,[1,5] Géraldine Laloux,[2] and Christine Jacobs-Wagner[1,5,6,7,8,*]
[1]Howard Hughes Medical Institute, Stanford University, Stanford, CA 94305, USA
[2]de Duve Institute, UCLouvain, Brussels, Belgium
[3]Department of Biology, KU Leuven, Leuven, Belgium
[4]Centre de Biologie Intégrative de Toulouse, Laboratoire de Microbiologie et Génétique Moléculaires, Université de Toulouse, Toulouse, France
[5]Department of Biology, Stanford University, Stanford, CA 94305, USA
[6]Sarafan Chemistry, Engineering Medicine for Human Health Institute, Stanford University, Stanford, CA 94305, USA
[7]Department of Microbiology and Immunology, Stanford School of Medicine, Stanford, CA 94305, USA
[8]Lead contact
*Correspondence: jacobs-wagner@stanford.edu
https://doi.org/10.1016/j.cels.2023.12.001

SUMMARY

To examine how bacteria achieve robust cell proliferation across diverse conditions, we developed a method that quantifies 77 cell morphological, cell cycle, and growth phenotypes of a fluorescently labeled *Escherichia coli* strain and >800 gene deletion derivatives under multiple nutrient conditions. This approach revealed extensive phenotypic plasticity and deviating mutant phenotypes were often nutrient dependent. From this broad phenotypic landscape emerged simple and robust unifying rules (laws) that connect DNA replication initiation, nucleoid segregation, FtsZ ring formation, and cell constriction to specific aspects of cell size (volume, length, or added length) at the population level. Furthermore, completion of cell division followed the initiation of cell constriction after a constant time delay across strains and nutrient conditions, identifying cell constriction as a key control point for cell size determination. Our work provides a population-level description of the governing principles by which *E. coli* integrates cell cycle processes and growth rate with cell size to achieve its robust proliferative capability.
A record of this paper's transparent peer review process is included in the supplemental information.

INTRODUCTION

Bacteria are notorious for their proliferative capabilities, which have direct implications in medicine, agriculture, and industry. Like all cells, bacteria must grow in size, replicate their DNA, segregate their genome, and divide to multiply. These processes must be coordinated to ensure faithful self-replication across all cells.[1] However, most bacteria, including the best-studied model *Escherichia coli*, seem to lack many of the cell cycle checkpoints and regulatory systems (e.g., cyclins, cyclin-dependent kinases, and the mammalian target of rapamycin [mTOR]) that ensure smooth cell cycle progression in eukaryotic cells.[2–4] Despite this, bacterial replication is remarkably faithful (i.e., virtually error-free), with each mother cell producing daughter cells that are themselves competent for self-replication. For many bacteria, cellular replication is also robust to environmental fluctuations. For instance, *E. coli* and other bacteria can multiply under a vast array of nutritional conditions, exhibiting large variations in doubling time (<20 min to days) and cell volume (up to 5-fold for a single species).[5–7] In fact, under nutrient-rich conditions, *E. coli* achieves the feat of dividing faster than it can replicate its genome by initiating DNA replication in one or two preceding division cycles.[8] Even then, cellular replication remains faithful.

How bacterial cells control cell cycle progression across diverse conditions is not well understood. In this study, we hypothesized that bacteria like *E. coli* are so adaptable because, on average, cells follow the same simple rules of cell cycle control across nutrient conditions and other perturbations. We propose to call such unifying rules "cell cycle laws," by analogy with the growth laws that have been proposed previously. A classic example is the nutrient-imposed growth law, which describes that the average cell volume (V) of a bacterial population scales exponentially with the average growth rate (α) across nutrient-rich conditions ($V \propto e^{\alpha T}$, with T a growth-rate-independent constant of ~1 h).[5,6] To our knowledge, the only proposed cell cycle law in bacteria applies to the initiation of DNA replication, which was first suggested in the 1960s.[9] It stipulates that at the population level, DNA replication initiates at a constant volume (V_i) per chromosomal origin of replication (*ori*). This cell cycle law was deduced from the nutrient-imposed growth law under the assumption that the C + D period (time of DNA replication + time between the end of DNA replication and cell division) is

This is an open access article under the CC BY license (http://creativecommons.org/licenses/by/4.0/).

constant.[9] However, this assumption only holds under the nutrient-rich (fast-growth) regime.[8] To account for the scaling of the C + D period with the generation time in nutrient-poor (slow-growth) conditions,[10–14] the nutrient-imposed growth law has recently been expanded to include a variable C + D period ($V \propto e^{\alpha*(C+D)} = 2^{(C+D)/\tau}$; with τ being the average doubling time).[14,15] This expanded relationship, referred to as the general growth law[14] hereafter, relates the average cell volume of a population to its average number of *ori* (given by $2^{(C+D)/\tau}$). The relation indicates a constant V_i/ori, as $V = V_0 * 2^{(C+D)/\tau}$ (with V_0, the average cell size per *ori* or the unit cell volume, being directly proportional to V_i/ori; $V_0 = V_i/ori * \ln(2)$).[14,15] However, this constancy of V_i/ori remains under debate as some studies support it,[13–19] whereas others do not.[20–25] This has also led to the proposal of an alternative relationship in which cell volume scales linearly with $\alpha * (C + D)$.[22]

Although the interplay between DNA replication initiation and cell size or growth rate has received much attention, it remains to be seen whether other cell cycle events follow unifying rules that reflect dependencies on cell size or growth rate. Below, we describe a large-scale phenotyping approach that allowed us to simultaneously extract quantitative features related to cell size, cell morphology, and cell cycle progression across a wide array of perturbations in *E. coli*. This high-content cell data combined with growth rate measurements enabled us to map the phenotypic space of cell morphogenesis, population growth, and cell cycle functions in *E. coli*. We first used this dataset to demonstrate that a wide range of independent perturbations is critical to identify robust population-level cell cycle laws. Besides testing previously proposed relationships, our analysis suggests four additional cell cycle laws that apply to different DNA- and division-related events. Although these laws only apply to the average behavior of *E. coli* (i.e., do not directly relate to the mechanisms at play at the single-cell level), they constrain the search for potential cellular mechanisms by linking specific cell cycle events to specific aspects of cell and nucleoid morphology. Finally, we also highlight the existence of mutant strains that consistently break these laws. Taken together, our study provides a population-level understanding of how *E. coli* robustly regulates and integrates cell cycle progression and growth rate through cell size-related governing principles.

RESULTS

Quantification of *E. coli* cell morphology and cell cycle events across nutrient conditions and large-scale genetic perturbations

To observe the interplay between cell morphology and different cell cycle events in *E. coli*, we used a strain harboring the following two chromosomally encoded fluorescent fusions: one to the divisome component FtsZ[26] and the other to the DNA replication marker SeqA[27] (Figure 1A). We grew this strain under 41 different carbon source conditions (Table S1; Figures 1B and S1A), giving rise to cultures of different average cell sizes (from ~1 to ~5 μm^3) and doubling times (from ~20 min to ~3 h). For each condition, we stained exponentially growing cells with the DNA dye DAPI to visualize the nucleoids. We developed a pipeline for quantitative image analysis to extract single-cell features and calculate population averages for all extracted features from phase contrast and fluorescence microscopy snapshots (Figure 1A; see STAR Methods). To determine the relative timings of each cell cycle event, we used an established method,[20,28–30] referred to here as the relative timing inference (RTI) method, which is based on the fraction of cells that have passed a specific cell cycle stage (Figure 1A). Several laboratories,[31–34] including ours (see STAR Methods), have verified this method through comparison with time-lapse experiments. We used this RTI approach in combination with the fluorescent markers (FtsZ-Venus^{SW}, SeqA-mCherry, and DAPI-stained nucleoids) to extract the relative timings of the following six cell cycle events: initiation and termination of DNA replication, FtsZ ring formation, initiation of cell constriction, initiation of nucleoid constriction, and nucleoid separation (Figures S1B–S1F; see STAR Methods). In parallel, we obtained growth rate measurements from population growth curves (Figure 1A; see STAR Methods), which were then used to transform relative cell cycle timings into absolute times (Dataset S1).

Modulating cell size by altering the nutrient composition of the growth medium is a valuable approach, but it has two limitations. First, regardless of the number of different media used, they all affect metabolism, and as such, they only represent one type of perturbation. Second, changes in nutrient quality result in correlated effects between growth rate and cell size,[5,6] preventing their uncoupling. To address these limitations and expand the phenotypic space, we used information from our previous genome-wide microscopy study of the *E. coli* Keio collection[35] to select 806 gene deletions associated with one or more alterations in cell/nucleoid morphogenesis and/or growth in M9 medium containing glucose, casamino acids, and thiamine (M9gluCAAT) (see STAR Methods). As before,[35] we verified the reproducibility of imaging and measurements (e.g., cell length and width) across these 806 gene deletions in M9 medium containing glycerol (M9gly) (Figure S1G; see also STAR Methods). Then, we individually transduced the gene deletions into our parent strain. Our subset of deletion strains was as diverse as the complete genome-wide library in terms of the distribution and number of different cellular processes that are impacted by the gene deletions (Figure 1C). Gene deletions that affect different processes effectively function as independent perturbations. This large number of independent and diverse perturbations enabled us to average out any specific effect conferred by a given mutation and confidently identify dependencies between the different features of the system.[35–38]

To further increase the sampling of the phenotypic diversity available to *E. coli*, we analyzed our mutant library in four different nutrient conditions (Figure 1D): an M9 buffer with L-alanine (M9Lala), glycerol (M9gly), glucose (M9glu), or L-arabinose with casamino acids and thiamine (M9LaraCAAT). The nutrient conditions varied substantially in carbon source quality, giving rise to different average growth rates, cell sizes, and DNA replication regimes (discrete vs. overlapping DNA replication cycles).[5,6,8] In total, we imaged approximately 4,300,000 individual cells, yielding 1,384 ± 380 cells/strain/nutrient condition. Quantification of cellular features and cell cycle timings revealed that this mutant library generated broad phenotypic diversity within each nutrient and, thus, metabolic condition, as

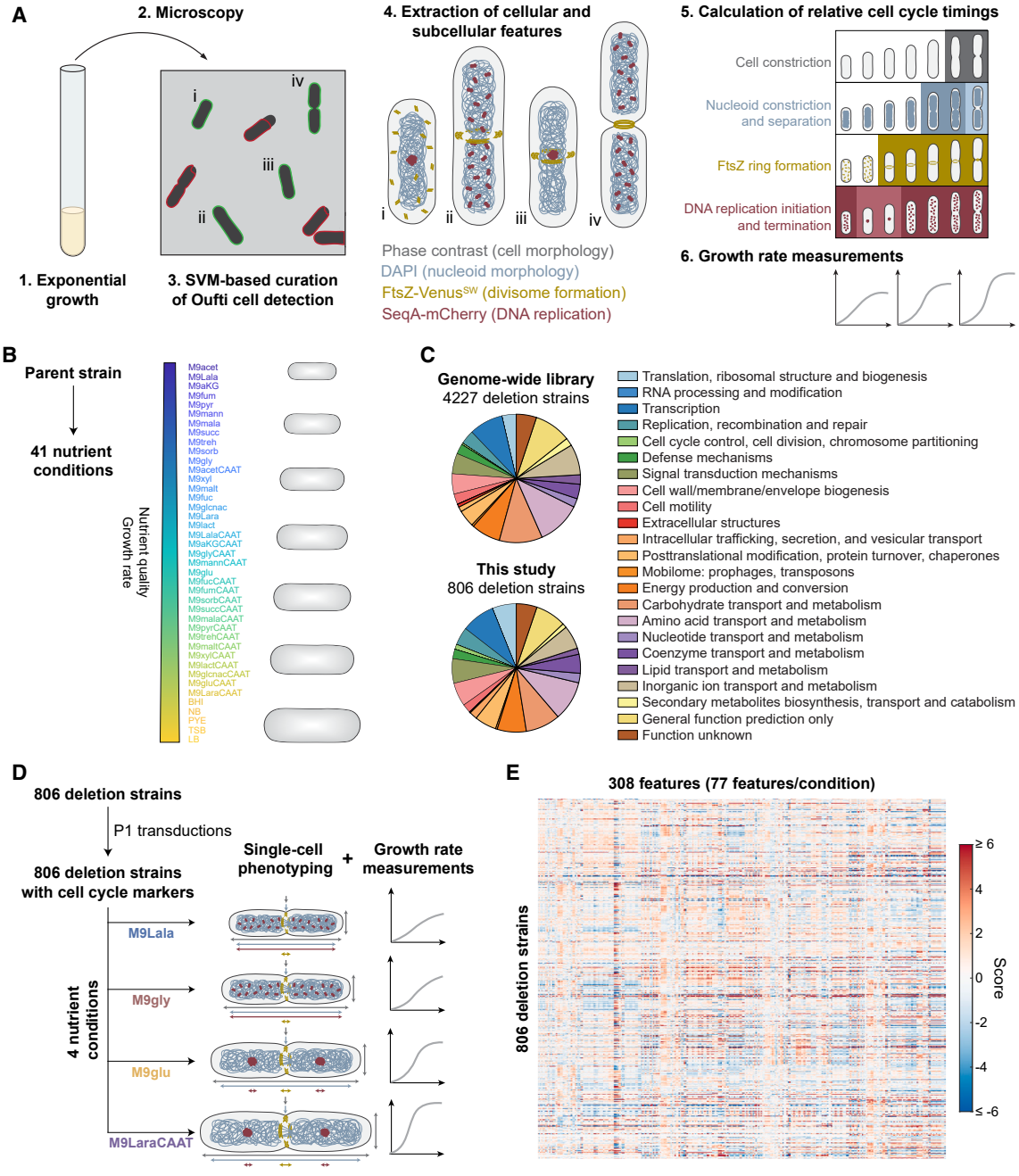

Figure 1. Experimental pipeline

(A) Schematic showing the experimental pipeline, including the different steps of the microscopy-based phenotyping approach and the population growth measurements.

(B) Schematic showing the 41 nutrient conditions (Table S1) in which the parent strain was grown. The media differ in carbon quality and give rise to different growth rates and cell sizes (Dataset S1).

(C) Pie charts representing the relative distribution of clusters of orthologous groups (COGs) categories among the gene deletion strains of the library used in this study versus those in the genome-wide Keio collection.

(D) Schematic showing the experimental approach for the generation and use of our gene deletion library, grown in four different nutrient conditions.

(E) Heatmap showing the feature scores (s) of the 806 deletion strains across the four nutrient conditions. The color scale is linear.

See also Figures S1 and S2.

illustrated with key features in Figures S2A and S2B. For comparison, we imaged ≥115 replicates of the parent strain under the same four nutrient conditions (Figure S2A).

In total, we measured 77 different average features for each deletion strain in each nutrient condition (Dataset S2). We also calculated a normalized score (s) for each feature of a strain in

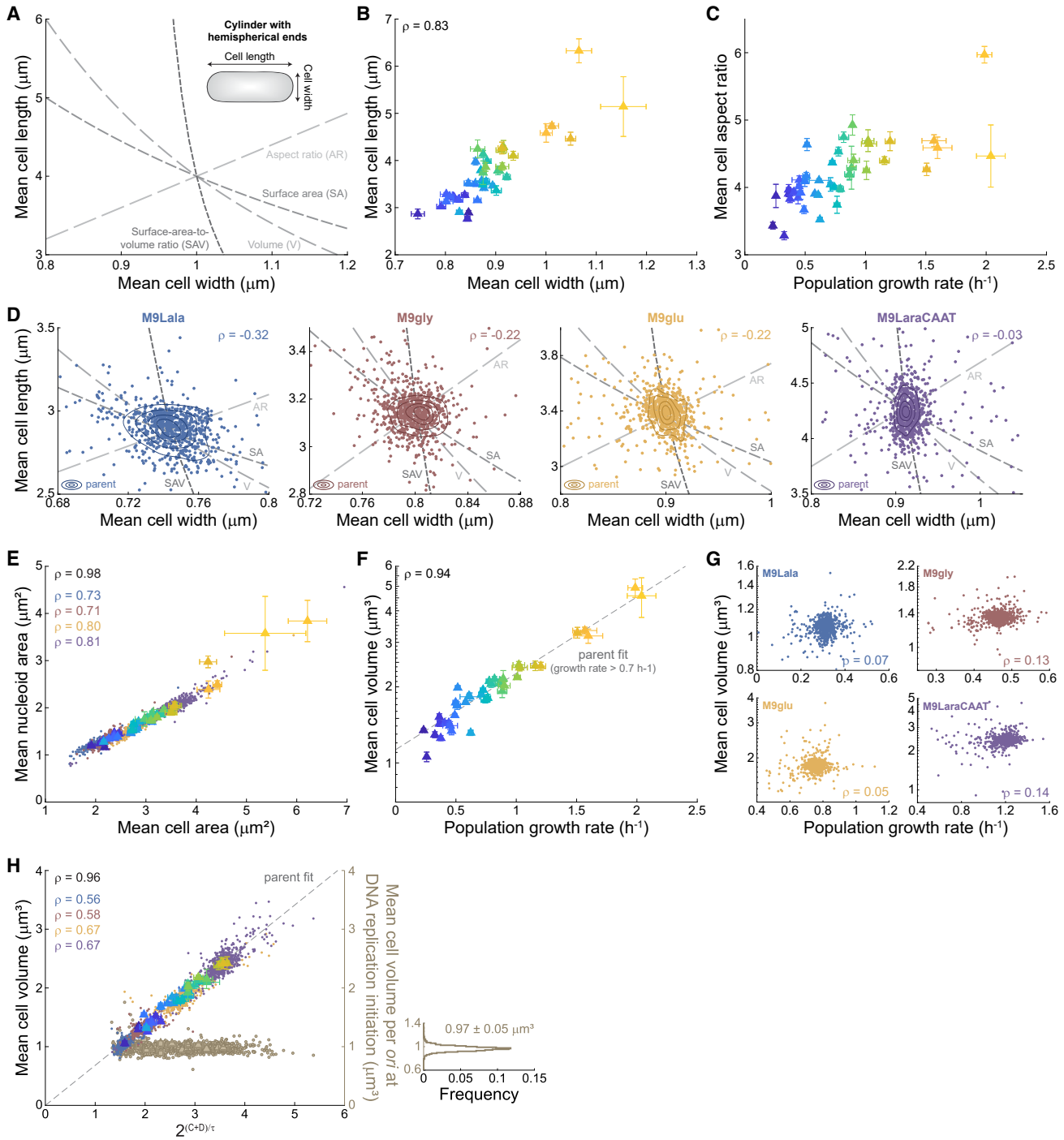

Figure 2. Examination of previously reported relationships

In all panels, triangles show the mean values of the indicated features for the parent strain across nutrient conditions (color-coded based on Figure 1B), with error bars indicating SD between individual experiments ($n \geq 4$). Small dots indicate the data for the deletion strains, colored according to the nutrient condition. The Spearman correlation coefficient (ρ) is shown for each colored data, with ρ in black showing the correlation for the parent strain data.

(A) Predicted relationships between cell length and width if cells (with an initial cell length of 4 μm and cell width of 1 μm) were to maintain a constant aspect ratio, surface area, volume, or surface-area-to-volume ratio. Cells were modeled as cylinders with hemispherical ends (inset).

(B) Scatterplot of mean cell length versus mean cell width for the parent strain across nutrient conditions.

(C) Scatterplot of mean cell aspect ratio versus population growth rate for the parent strain across nutrient conditions.

(D) Scatterplots of mean cell length versus mean cell width for the gene deletion strains. Each panel shows a different nutrient condition. Isocontours represent the 0.10, 0.25, 0.50, and 0.75 probability envelopes of the parent replicates in the same nutrient condition. Shown in gray are the predicted relationships between cell

(legend continued on next page)

each nutrient condition (see STAR Methods; Dataset S2). This score represents the extent to which a mutant strain deviates from the parent replicates in terms of standard deviations (SDs) away from the median. As such, the scores allow the determination and visualization of the variability in cellular features that were sampled across our dataset (Figure 1E). We wish to emphasize that all extracted cellular features are population averages (i.e., means) and do not directly apply to single-cell level behavior. From hereafter, any reference to a cellular feature refers to a population average.

Cell length and width do not co-vary across large-scale perturbations

We first examined the average behavior of cells with respect to cell size and shape control. This question has been the subject of many studies in *E. coli* and other microbes. However, these investigations have led to conflicting conclusions about which dimensions of cell morphology (cell length,[39,40] volume,[19,41] surface area,[42] the surface-area-to-volume ratio,[43–45] or aspect ratio[46]) are kept constant on average.[35,47] These studies employed either a small number of perturbations (genetic, chemical, or metabolic) or specific perturbations (targeting only a single protein or a small subset of proteins). Therefore, we used our large dataset of measurements (Dataset S2) to revisit this biological question by examining the relationship between cell length and width across perturbations. A constant aspect ratio predicts a positive relationship between cell length and width, whereas we expect different negative relationships for a constant cell volume, surface area, or surface-area-to-volume ratio, as depicted by the dashed lines in Figure 2A.

Across nutrient conditions, it is well known that both the length and width of *E. coli* cells increase with increasing growth rate,[5,39,48] leading to a positive correlation between the two variables (Figure 2B). Despite this positive correlation, we did not observe a constant cell aspect ratio across nutrient conditions for the parent strain (Figure 2C). We also found no positive relationship between cell length and width across deletion strains, irrespective of the nutrient condition (Figure 2D). The Spearman correlation (ρ) between cell length and width was close to zero in the nutrient-rich medium (M9LaraCAAT), consistent with our genome-wide study,[35] and weakly negative in the nutrient-poorer media (M9Lala, M9gly, and M9glu). Regardless of the growth medium, the data collectively failed to follow any specific relationship (shown by the dashed lines in Figure 2D) that would argue for cell size sensing through surface area, volume, or the ratio of the two. These findings illustrate the importance of sampling large numbers and different types of perturbations to test general relationships.

Nucleoid length robustly scales with cell length

Although the relationship between cell length and width widely differed across strains and nutrient conditions, other features exhibited more consistent behavior. In agreement with a scaling relation between nucleoid and cell size,[35,49,50] we observed a strong positive correlation between nucleoid and cell areas across all data (Figure 2E). Nucleoid length displayed a stronger linear relationship with cell length than nucleoid width with cell width (Figures S3A and S3B), suggesting that nucleoid length scaling is the main driver behind the overall size scaling of the nucleoid.

DNA replication initiates at a constant cell volume per *ori*

Our dataset also allowed us to revisit debated bacterial laws. First, we confirmed a recent report[22] that the nutrient growth law (i.e., the exponential scaling between cell volume and growth rate) becomes less reliable in nutrient-poor conditions ($\alpha < 0.7\ h^{-1}$) with cells becoming smaller than predicted based on their growth rates (Figure 2F). In addition, we observed no correlation between cell volume and growth rate for the deletion strains within the four nutrient conditions (Figure 2G), which is consistent with our previous study.[35] Growth rate was also uncorrelated with other morphological variables such as cell surface area and surface-area-to-volume ratio (Figures S3C and S3D).

On the other hand, the recently challenged general growth law in which cell volume scales linearly with the average number of *ori* (given by $2^{(C+D)/\tau}$)[14,15] did hold across all perturbations, with data points from both the parent and deletion strains collapsing onto the same curve (Figure 2H). In contrast, the proposed alternative between cell volume and $\alpha * (C + D)$[22] did not yield the expected linear relationship (Figure S3E). The agreement of our data with the general growth law indicates that the mean cell volume per *ori* at DNA replication initiation remains largely constant across strains and nutrient conditions ($0.97 \pm 0.05\ \mu m^3$, mean ± SD, n = 3,137 perturbations) (Figure 2H). This average population rule has long been debated (Table S2). Comparison of our data with four recent available datasets with pertinent data[14,22,51,52] revealed that all but one agree with a largely constant DNA replication initiation volume per *ori* (Figures S3F–S3H). Although the exact values differ across datasets because of different image analysis approaches and parameters, the constancy across nutrient conditions is largely conserved (Figures S3F–S3H). While the measurement precision of earlier studies providing support for a constant V_i/ori has been questioned,[22] our measurements were highly reproducible across replicates of the parent strain in the 36 tested nutrient conditions, as shown by the small SDs (Figure S3F). Furthermore, our study uses the largest number of diverse perturbations among studies that have examined the

length and width if cells were to maintain an aspect ratio (AR), surface area (SA), volume (V), or surface-area-to-volume (SAV) ratio equal to that of the parent strain in the same nutrient conditions. Panel axes were cropped to remove outliers and more clearly show most of the data.

(E) Scatterplot of mean nucleoid area versus mean cell area for both parent and deletion strains across nutrient conditions.

(F) Scatterplot of mean cell volume versus growth rate for the parent strain across nutrient conditions. The dotted gray line shows an unconstrained linear fit for growth rates > $0.7\ h^{-1}$.

(G) Scatterplots of mean cell volume versus growth rate for the deletion strains in each nutrient condition.

(H) Scatterplot of mean cell volume versus the average number of *ori* (given by $2^{(C+D)/\tau}$). The dotted gray line shows a linear fit of the parent data across nutrient conditions (with the intercept constrained to the origin). Scatterplot of the mean cell volume per *ori* at initiation of DNA replication versus the average number of *ori* is shown in beige. The frequency distribution of cell volumes per *ori* at the initiation of DNA replication, combining all measurements, is shown on the right. Mean ± SD is indicated on the plot.

See also Figure S3.

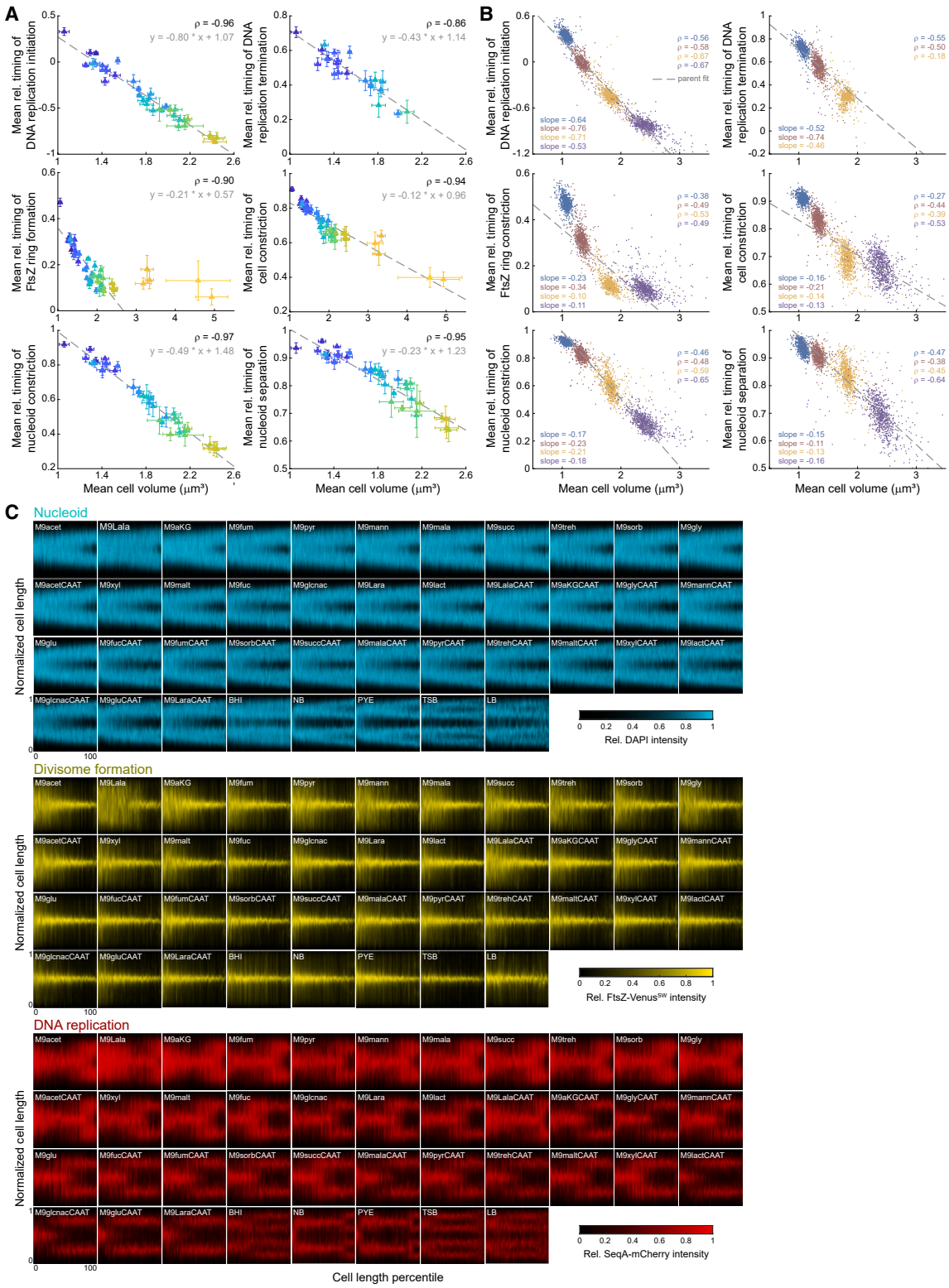

Figure 3. Cell size dependence of the timing of cell cycle events

(A) Scatterplots of the relative timing of the indicated cell cycle events versus mean cell volume for the parent strain across nutrient conditions (color-coded based on Figure 1B), with the error bars indicating SD between individual experiments ($n \geq 4$). ρ = Spearman correlation coefficient. The dotted gray line indicates the unconstrained linear fit of the parent strain data across nutrient conditions. For FtsZ ring formation, the linear fit was constrained to exclude the five richest nutrient conditions (lysogeny broth [LB], tryptic soy broth [TSB], peptone yeast extract broth [PYE], nutrient broth [NB], and brain heart infusion [BHI]). For these five

(legend continued on next page)

relation between DNA replication initiation and average cell size (Table S2). We note that only the cell volume at DNA replication initiation per *ori*, and not cell length, area, or surface area (Figure S3H), was generally constant across strains and conditions. This indicates that, at the population level, initiation of DNA replication in *E. coli* is coupled to cell volume and no other cell morphological feature, similar to in *Bacillus subtilis*.[53]

The relative timing of cell cycle events negatively correlates with cell size

To examine whether similar principles exist for other cell cycle events, we first plotted the relative cell cycle timings of the parent strain versus its average cell volume or growth rate across nutrient conditions in which they could be extracted. Although variable timings, across cell volumes or growth rates, have been reported for nucleoid separation,[25,35,54,55] FtsZ ring formation,[56–58] and cell constriction,[35,54,58,59] no unifying rules have been identified. For all cell cycle events but FtsZ ring formation (see below), we found a strong negative, linear dependency with cell volume (Figure 3A) and, to a lesser extent, with growth rate (Figure S4A). These linear relationships are valuable for their predictive power. They enable the inference of any cell cycle timing (initiation of cell constriction, initiation and termination of DNA replication, initiation of nucleoid constriction, and separation of nucleoids) for the parent strain based on a simple cell volume measurement of the population in any given nutrient condition. Similarly, determination of a single relative timing (e.g., initiation of cell constriction) allows inference of not only the average cell volume but also the timing of any other cell cycle event (e.g., termination of DNA replication or nucleoid separation). However, these empirical relationships appeared to only apply to metabolic changes, as the mutant data deviated to varying degrees (Figure 3B). Deletion strains with larger cells tended to execute cell cycle events earlier in the cell cycle, as shown by the negative ρ values across deletion strains under the same nutrient condition (Figure 3B). Since such a negative correlation was not observed for growth rate ($\rho \sim 0$, Figure S4B), these results suggest a form of cell size control for all examined cell cycle events.

To examine this connection with cell size, we tested all pairwise relationships between each cell cycle event's relative or absolute timing and all other features across strains and nutrient conditions. In some cases, we could not reliably extract some cell cycle timings in the richest media (see STAR Methods). Despite this limitation, our dataset remained rich in variability as evidenced by the wide range of absolute and relative timings obtained for each cell cycle event (Figures 3A and 3B). Furthermore, when needed, we used demographs of the DAPI, SeqA-mCherry, and FtsZ-Venus^{SW} signals to extract qualitative information (see below). Such demographs consist of linear representations of integrated fluorescence of cells sorted by their length.[60] They provide an overview of DNA replication, nucleoid, and FtsZ dynamics along the cell division cycle across media (Figure 3C). Our goal was to identify cell cycle laws, i.e., population-level governing principles that apply across strains and nutrient conditions. Specifically, we focused on identifying features that remained relatively constant in relation to a specific cell cycle event across the many genetic and metabolic perturbations that we introduced, similar to the constant volume per *ori* at initiation of DNA replication. From this extensive analysis emerged four additional laws, one per cell cycle event discussed below.

Nucleoid constriction occurs at a constant nucleoid length

In our study, the onset of nucleoid constriction marked the first visible step of bulk chromosome segregation. This step varied in timing across our dataset, ranging from 0.2 to 0.9 in relative cell cycle time and ~10 min to > 2.5 h in absolute time (Figure 4A). Within this broad range, nucleoid constriction occurred at a relatively constant nucleoid length (3.20 ± 0.25 μm, n = 3,161 perturbations, Figure 4B). Nucleoid constriction also tended to initiate at a constant cell length (3.89 ± 0.31 μm, Figure 4C), given the scaling between nucleoid length and cell length (Figure S3A).

The order of cell cycle events changes with the nutrient quality

Next, we examined cell division events, starting with the earliest one we observed: FtsZ ring formation. Unlike DNA-related events, FtsZ ring formation only showed a negative correlation with cell volume in nutrient-poor conditions (Figure 3A). This was because FtsZ ring formation is limited to one per division cycle, as illustrated in FtsZ-Venus^{SW} demographs of the parent strain across nutrient conditions (Figure 3C). These demographs confirmed that the accumulation of FtsZ-Venus^{SW} at midcell, which marks the formation of the FtsZ ring, occurs later in poor media relative to richer media. However, even in the richest nutrient conditions (Figure 3C), these demographs showed no clear evidence of additional FtsZ rings at the ¼ and ¾ positions (which would become midcell positions in the future daughter cells). This indicates that the number of FtsZ rings is constrained to one per generation. Because of this "generational constraint," the relative timing of FtsZ ring assembly at midcell reached a plateau near the beginning of the cell cycle in media where populations have a mean cell volume $\gtrsim 2\ \mu m^3$ (Figure 5A). In contrast and as expected, initiation of DNA replication could often be traced back to the previous generation in richer nutrient

conditions, timings for DNA replication and nucleoid constriction or separation could also not be reliably extracted (see STAR Methods). The relative timing of DNA replication termination could not be determined in rich nutrient conditions in which cells displayed overlapping rounds of DNA replication (see STAR Methods).

(B) Same as (A) but for the deletion strains across nutrient conditions. Colors indicate the nutrient condition in which strains were imaged. The dotted gray lines correspond to the linear fits for the parent data shown in (A). Note that we were unable to extract timings of DNA replication termination for deletion strains in M9LaraCAAT (data usually in purple) due to the presence of overlapping DNA replication forks.

(C) Demographs of DAPI, FtsZ-Venus^{SW}, and SeqA-mCherry signals in the parent strain across the indicated nutrient conditions, showing nucleoid dynamics, divisome formation and DNA replication characteristics, respectively. Cell length is normalized to show the relative cell length in the y axis. Nutrient conditions were ordered based on increasing growth rate. The color scales are linear and indicate the relative fluorescent intensities of the different signals.

See also Figure S4.

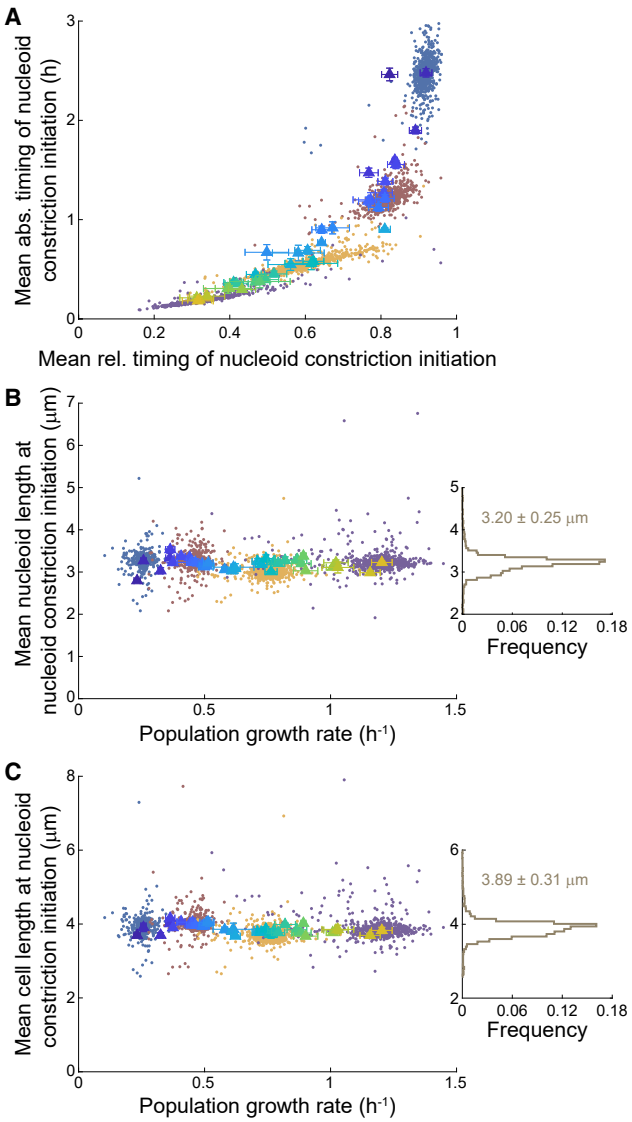

Figure 4. Constant nucleoid length at nucleoid constriction

In all panels, triangles show the mean values of the indicated features for the parent strain across nutrient conditions (color-coded based on Figure 1B), with the error bars indicating SD between individual experiments ($n \geq 4$). Small dots indicate the data for the deletion strains, colored according to the nutrient condition. The Spearman correlation coefficient (ρ) is shown for each colored data, with ρ in black showing the correlation for the parent strain data. Initiation of nucleoid constriction could not be reliably determined in the five richest nutrient conditions (LB, TSB, PYE, NB, and BHI) because it occurred in the previous generation.

(A) Scatterplot of the absolute time from birth to nucleoid constriction initiation versus the relative timing of nucleoid constriction initiation.

(B) Scatterplot of the nucleoid length at nucleoid constriction initiation versus growth rate. The frequency distribution of nucleoid lengths at nucleoid constriction initiation, combining all measurements, is shown on the right. Mean ± SD is indicated on the plot.

(C) Scatterplot of the cell length at nucleoid constriction initiation versus growth rate. The frequency distribution of cell lengths at nucleoid constriction initiation, combining all measurements, is shown on the right. Mean ± SD is indicated on the plot.

See also Figures S8 and S10.

conditions (Figure 5A). Analysis of the parent strain demographs also revealed that in the five richest conditions, DNA replication initiated two generations prior (as evidenced by the appearance of four separate signals; Figure 3C). Similarly, nucleoid separation could also occur in a previous generation. This was showcased in DAPI demographs of the parent strain grown in the richest nutrient conditions, where cells were already born with two separated nucleoids (Figure 3C), as described before.[54]

The absence of a generational constraint for DNA-related events resulted in a change in the order of cell cycle events when populations reached a mean cell volume of ~3 μm^3 (growth rate of ~1.5 h^{-1}). FtsZ ring formation at midcell switched from preceding nucleoid constriction and separation to following these DNA-related events in the richest media where these events happened in the previous generation (Figure 5B). Similarly, because of its dependence on FtsZ ring formation, cell constriction changed from almost coinciding with nucleoid constriction (Figure S5A) and preceding nucleoid separation to becoming the last cell cycle event to occur in the richest media (Figure 5B).

FtsZ ring forms only once per generation and above a constant cell length threshold

The switch in event order was surprising, given the common belief that a FtsZ ring cannot form until after the nucleoid has constricted to create DNA-free space at the middle of the cell,[61–63] a phenomenon often referred to as nucleoid occlusion. Although the term "nucleoid occlusion" has been used to describe the inability of FtsZ rings to either form or constrict over unsegregated chromosomes,[64–66] the commonly assumed role of nucleoid occlusion in FtsZ ring formation stems from the original identification of nucleoid occlusion factors that were reported to inhibit FtsZ ring assembly in the vicinity of the bacterial chromosome.[63,67] These studies were done in rich growth media. However, we found that outside the five richest media, FtsZ ring formation preceded nucleoid constriction in the other 36 tested media (Figure 5B), leading to the emergence of many cells (>30%) with a FtsZ ring over an unconstricted nucleoid (Figures 5C and 5D). Thus, nucleoid occlusion does not appear to be a robust inhibitory mechanism for FtsZ ring formation across nutrient conditions.

Although FtsZ ring formation occurred almost immediately following cell birth in rich media associated with mean cell volumes > 2 μm^3 (doubling time < 1 h), the timing of this cell cycle event varied dramatically in nutrient-poorer conditions, from almost right away to over 2 h after cell birth (Figure 5E). This variability was not due to differences in FtsZ amount or concentration within the cells, as these variables displayed little to no correlation with the relative or absolute timing of FtsZ ring formation (Figure S5B). Instead, in these nutrient-poorer conditions (doubling time > 1 h), we found that FtsZ ring formation occurred at a relatively constant cell length (2.84 ± 0.28 μm, n = 1,583 perturbations; Figure 5F). Together with the observation of the generational constraint (Figures 3C, 5A, and 5E), these results suggest that FtsZ ring formation follows a two-rule principle: FtsZ forms a ring (1) only once per division cycle and (2) after a certain length threshold has been reached if the generational constraint is not at play (i.e., in nutrient-poorer conditions). Both criteria must be met, regardless of the conditions (poor or rich). Although this two-rule principle is unifying across nutrient conditions, it leads to the appearance of a different behavior between slow and fast

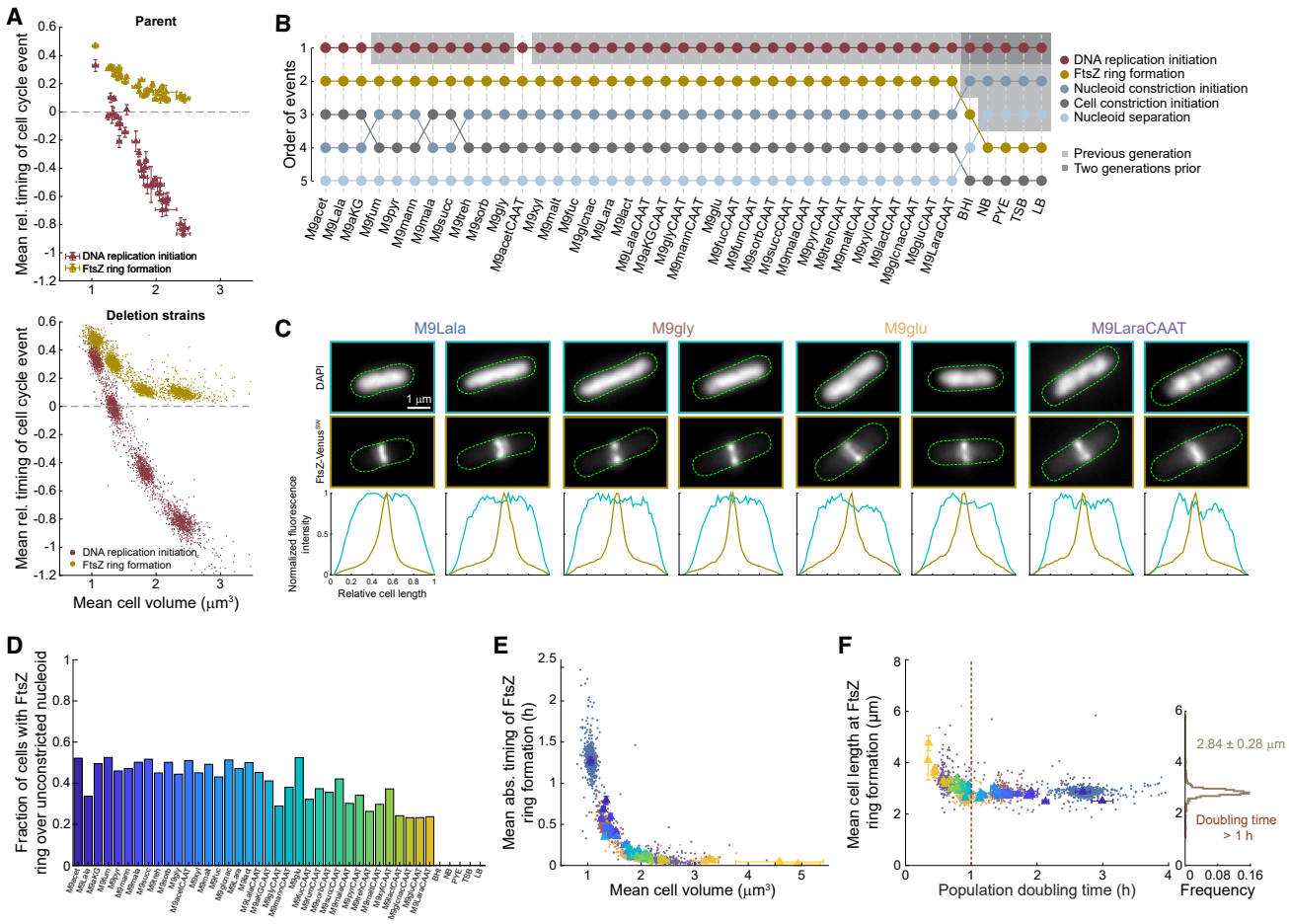

Figure 5. Generational constraint and cell length threshold of FtsZ ring formation

(A) Scatterplot of the relative timing of FtsZ ring formation and DNA replication initiation for the parent strain (top) and deletion strains (bottom) versus mean cell volume across nutrient conditions. Error bars indicate SD between individual experiments ($n \geq 4$). Negative values indicate that the cell cycle event occurred one or two generations prior.

(B) Relative order of cell cycle events across nutrient conditions for the parent strain. Nutrient conditions were ordered based on increasing growth rate. Shadings indicate cell cycle events that occurred one (light gray) or two generations (dark gray) prior.

(C) Top, representative fluorescence images of the parent strain in the indicated nutrient conditions. Bottom, fluorescence intensity profiles of DAPI and FtsZ-Venus^{SW} signals for these cells.

(D) Bar graph showing the fraction of cells with a FtsZ ring over an unconstricted nucleoid across nutrient conditions (ordered based on increasing growth rate).

(E) Scatterplot of the absolute timing of midcell FtsZ ring formation versus cell volume. Triangles show the mean values of the parent strain across nutrient conditions (color-coded based on Figure 1B). Error bars indicate SD between individual experiments ($n \geq 4$). Small dots indicate the data for the deletion strains, colored according to the nutrient condition.

(F) Scatterplot of cell length at FtsZ ring formation versus doubling time. Triangles show the mean values of the parent strain across nutrient conditions (color-coded based on Figure 1B). Error bars indicate SD between individual experiments ($n \geq 4$). Small dots indicate the data for the deletion strains, colored according to the nutrient condition. The frequency distribution of cell lengths at FtsZ ring formation, for strains and nutrient conditions giving rise to a doubling time > 1 h, is shown on the right. Mean ± SD are indicated on the plot.

See also Figures S5 and S9.

nutrient conditions. In nutrient-poor conditions, the FtsZ ring forms, on average, at a constant cell length. In nutrient-rich conditions, cells are larger such that the length threshold is reached in the previous generation and the generational constraint delays FtsZ ring formation until after completion of cell division.

Cell constriction occurs after a constant cell length has been added

FtsZ ring formation is often explicitly or implicitly considered the main control point for cell division and, by extension, cell size determination. This raises the question of whether FtsZ ring formation triggers a temporal sequence of biochemical events (divisome assembly) that leads to cell constriction. Therefore, we examined whether there was a constant absolute or relative time between FtsZ ring formation and cell constriction. Such constant relative or absolute times between two events can be identified by plotting the average relative or absolute timing of these events across strains and nutrient conditions. If two cell cycle events were separated by a constant time, they would display a positive linear relationship with a slope of 1 and an intercept (x = 0) corresponding to

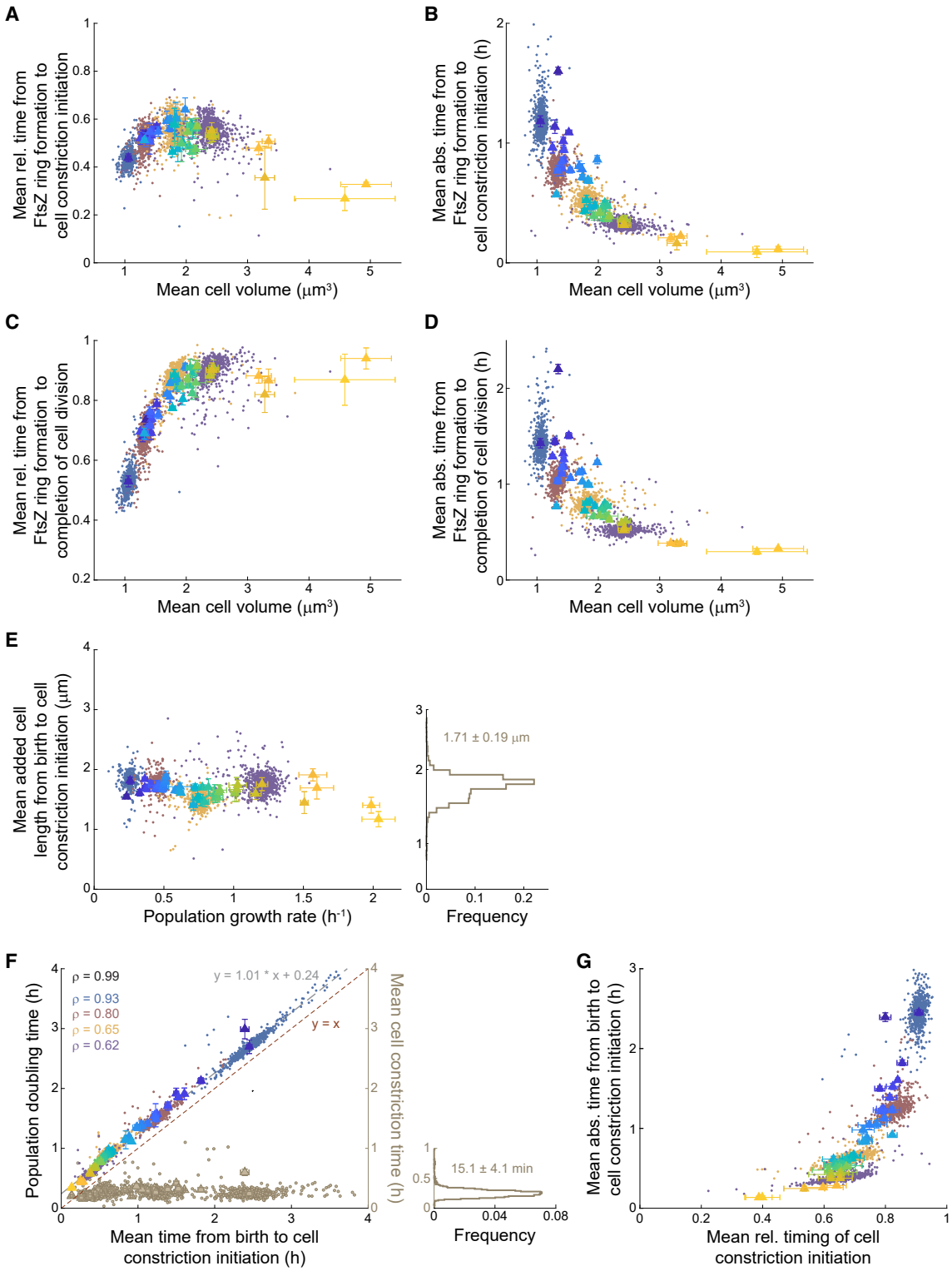

Figure 6. Cell constriction as a control point for cell size determination

In all panels, triangles show the means of the indicated features for the parent strain across nutrient conditions (color-coded based on Figure 1B), with the error bars indicating SD between individual experiments ($n \geq 4$). Small dots indicate the data for the deletion strains, colored according to the nutrient condition.

(A) Scatterplot of the relative time from FtsZ ring formation to cell constriction initiation versus cell volume.

(B) Scatterplot of the absolute time from FtsZ ring formation to cell constriction initiation versus cell volume.

(C) Scatterplot of the relative time from FtsZ ring formation to completion of cell division versus cell volume.

(legend continued on next page)

the average time delay between the two events. We found no evidence of a constant time between FtsZ ring formation and the onset of cell constriction (slope ≠ 1; Figure S6A). Instead, the relative and absolute time delays between these events varied across conditions (Figures 6A and 6B). Similar observations were made for the relationship between FtsZ ring formation and the completion of cell division (Figures 6C and 6D).

For the initiation of cell constriction, the closest principle of constancy we identified across strains and nutrient conditions was a fairly constant added cell length between birth and cell constriction (Figure 6E). Although we observed some variability, the distribution of added lengths between birth and cell constriction was relatively narrow (1.71 ± 0.19 μm, n = 3,166 perturbations) across strains and conditions compared with the wide range of average cell lengths (from ~3 to ~6 μm) (Figure 6E). This suggests that at the population level, cell constriction initiation tends to occur after a constant cell length has been added after birth.

Cell division follows cell constriction after a constant time delay

The least variable time delay we observed between any cell cycle events was between constriction initiation and cell separation. This was evident by (1) the high positive correlation between cell constriction initiation and doubling time and (2) the collapse of the data on a linear relationship with a slope of 1 and an intercept of 0.24 h (Figure 6F). This means that completion of cell division follows the initiation of cell constriction after a constant average time (~15 min at 37°C, n = 3,083 perturbations; Figure 6F). There was some variability in this time delay, with a few outliers across nutrient conditions (e.g., parent strain in M9acet) and deletion strains (Figure 6F). Regardless, the distribution of the time window remained small (SD = 4.1 min) across strains and media compared with the wide range of doubling times (from 20 min to 4 h). As a result of a relatively constant delay between cell constriction and separation, the timing of initiation of cell constriction happened early in the cell division cycle of fast-growing strains and late in slow-growing ones (Figure 6G). This also means that cell constriction takes up ~75% of the cell division cycle in nutrient-rich versus only ~6% in nutrient-poor conditions. A constant constriction time also argues that the initiation of cell constriction is a key control point for cell size determination.

The nutritional environment predominantly contributes to the phenotypic landscape

Although most deletion strains abide by the cell cycle laws proposed above, we identified mutants that significantly deviate from each law. There were two types of outliers depending on whether the mutant phenotype depended on the nutrient condition. The most common type was the nutrient-dependent outliers, which were defined by having $s > 3$ (or $s < -3$) for at least one nutrient condition and $s < 1.5$ (or $s > -1.5$) in at least one other condition (Figure 7A). In other words, these mutants broke the rule (i.e., deviated by at least three SD from the parent's median value) under some nutrient conditions but either behaved similarly to the parent (typically) or deviated from the parent in the opposite direction (rarely) under other nutrient conditions. Note that, in this analysis, we did not consider the cell length threshold principle for FtsZ ring formation because phenotypic robustness could only be assessed under two, instead of four, nutrient conditions due to the generational constraint in the two richest media (Figures 5E and 5F).

Nutrient-dependent phenotypes were not limited to the biological laws we identified. They were also common for all 77 features quantified in our study (Figure 7B). For example, for cell length, we identified 195 strains (24% of all gene deletion strains) that were significantly longer or shorter than the parent ($s > 3$ or $s < -3$) in at least one nutrient condition (expected false discovery rate of 1.2%), but the majority of them (156 strains) also displayed either parent-like cell lengths or deviations in the other direction ($s < 1.5$ or $s > -1.5$) in at least one other condition. A similarly large fraction of nutrient-dependent deviating phenotypes were observed for all other features (Figure 7B). To illustrate, Figure S7 shows an example of a nutrient-dependent phenotype with the Δ*clpX* strain (Figure S7A), which displayed minicell formation in nutrient-poor conditions (M9Lala and M9gly) but not in richer nutrient conditions (M9glu and M9LaraCAAT). These minicells, which are small anucleate cells produced by aberrant cell divisions at the cell poles,[68] were likely formed by perturbing the normal interaction between the ClpXP protease complex, the Min system, and FtsZ.[69,70] In line with these observations, the Δ*clpP* strain displayed a similar and even more severe nutrient-dependent phenotype, from dividing normally in M9LaraCAAT to producing minicells in M9gly and M9glu to not growing in M9Lala (Figure S7A; Dataset S2). The predominance of nutrient-dependent phenotypes across features (Figures 7A and 7B) suggests an important role for the nutrient condition and, more broadly, central metabolism in modulating the integration of cell cycle progression with cell morphogenesis and growth rate.

True rule breakers are rare

A small but important subset of outliers was nutrient independent (Figure 7C). Many of the genes deleted in these strains encode proteins that localize to either the cell envelope or the nucleoid (Figure 7C), stressing the importance of these two structures in cell replication. Among mutants that displayed a deviating phenotype across nutrient conditions (regardless of the direction), many still followed a rule of constancy reasonably well. Consider, for example, all mutants with an $|s| > 2$

(D) Scatterplot of the absolute time from FtsZ ring formation to completion of cell division versus cell volume.
(E) Scatterplot of the added cell length from birth to cell constriction initiation versus growth rate. The frequency distribution of added cell lengths from birth to cell constriction initiation, combining all measurements, is shown on the right. Mean ± SD are indicated on the plot.
(F) Scatterplot of doubling time versus the time from birth to cell constriction initiation. The dotted gray line indicates the unconstrained linear fit of all data across strains and nutrient conditions. The dotted red line represents the bisector (y = x), where data points would collapse if both events coincided. The Spearman correlation coefficient (ρ) is shown for each colored data, with ρ in black showing the correlation for the parent strain data. Scatterplot of the time from initiation of cell constriction to completion of cell division (i.e., the cell constriction time) versus the time from birth to cell constriction initiation is shown in beige. The frequency distribution of cell constriction times, combining all measurements, is shown on the right. Mean ± SD are indicated on the plot.
(G) Scatterplot of the absolute time from birth to cell constriction initiation versus the relative timing of cell constriction initiation.
See also Figures S6, S8, and S10.

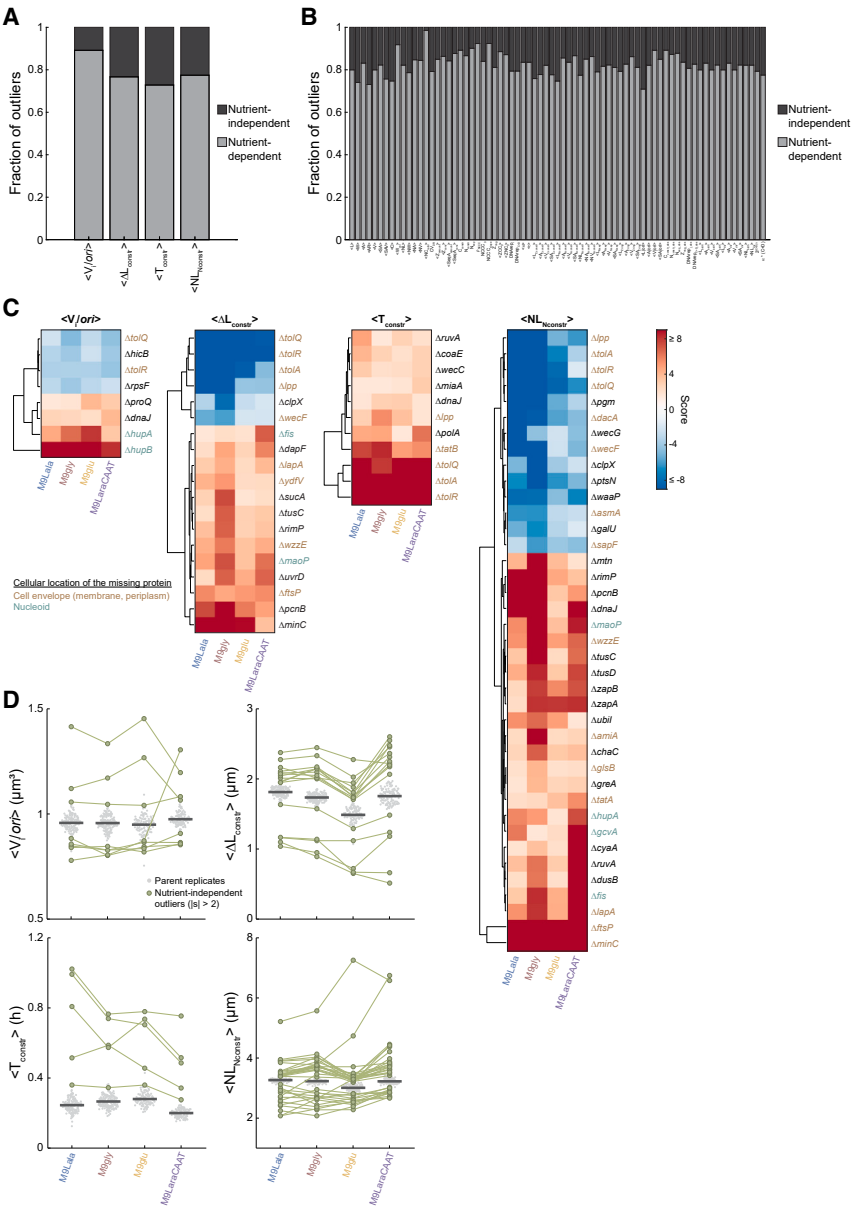

Figure 7. Rule breakers and nutrient-dependent phenotypic landscapes

(A) Bar graphs showing the fraction of nutrient-independent and -dependent outliers for the following cell cycle laws: constant mean DNA replication initiation volume per *ori* (V_i/ori), constant added mean cell length between birth and cell constriction (ΔL_{constr}), constant mean time between initiation and completion of cell constriction (T_{constr}), and constant mean nucleoid length at initiation of nucleoid constriction ($NL_{Nconstr}$). Nutrient-dependent outliers were defined by having $s > 3$ (or $s < -3$) for at least one nutrient condition but $s < 1.5$ (or $s > -1.5$) in at least one other condition. Nutrient-independent outliers were defined as having $s > 3$ (or $s < -3$) for at least one nutrient condition and $s > 1.5$ (or $s < -1.5$) in all other conditions. The strains that were identified as outliers (nutrient-dependent or -independent, $|s| > 3$ for at least one nutrient condition) represent 13.8%, 12.8%, 8.7%, and 26.4% of examined deletion strains for V_i/ori, ΔL_{constr}, T_{constr}, and $NL_{Nconstr}$, respectively.

(B) Bar graphs showing the fraction of nutrient-independent and -dependent outliers for 73 extracted population-level features (see Table S6 for the definition of symbols). Four features were omitted ($DNArep_C$, $DNArep_D$, $DNArep_{C\_abs}$, and $DNArep_{D\_abs}$) as these could not be reliably extracted in all four nutrient conditions (see STAR Methods).

(C) Clustergrams showing the normalized scores of nutrient-independent outliers for the indicated cell cycle laws. The color scale is linear.

(D) Outliers (green) with $|s| \geq 2$ across the four tested nutrient conditions for the indicated cell cycle laws. Parent replicates are shown as beeswarm plots in gray. Dark gray lines indicate the mean of parent replicates in each nutrient condition.

See also Figure S7.

for nucleoid constriction across the four tested media. Most of these mutants still initiated cell constriction at a similar mean nucleoid length (<$NL_{Nconstr}$>) in all four nutrient conditions, only at a lower or higher value relative to the parent (Figure 7D). Only a few gene deletion strains broke the rule of constancy by displaying large differences in values across conditions (Figure 7D). The scarcity of true rule breakers demonstrates how robust the rules of constancy are to the cellular replication of *E. coli*.

DISCUSSION

E. coli follows simple rules of cell cycle control at the population level

By phenotyping growth, cell cycle, and cell morphological features across large-scale perturbations, we show that *E. coli* follows unifying principles of cell cycle control at the population level. The proposed cell cycle laws are all connected to some aspect of cellular morphology, explaining the observed cell size dependence of cell cycle events (Figures 3A and 3B). Our results suggest that cell size dependence is achieved through different means depending on the cell cycle event. For instance, at the population level, initiation of DNA replication is coupled to a constant average cell volume per *ori* (Figure 2H), whereas FtsZ ring formation is connected to cell length (Figure 5F). Nucleoid constriction also appears connected to cell length (Figures 4B and 4C), consistent with an early report of a cell length threshold for nucleoid separation in spherical *rod* mutant cells,[71] by virtue of the scaling between nucleoid length and cell length (Figure S3A). For the initiation of cell constriction, we found no evidence for a mean cell size threshold or a constant delay relative to other cell cycle events. Instead, our analysis is more consistent with a control that relies on an average added cell length from cell birth (Figure 6E). Completion of cell division then follows the onset of cell constriction after a constant average time (Figure 6F). Our analysis of an existing dataset[54] further validated these constriction-related cell cycle laws and

confirmed that these findings are robust to the way that cell constriction is determined (see STAR Methods and Figures S6B–S6D). For the final step of cell division, the cell size regulation occurs indirectly via a dependence on cell constriction. This is in line with a recent report that used causal inference to demonstrate that the onset of cell constriction acts as a cell cycle checkpoint that controls cell size at division.[72] We propose that these simple governing principles emerge from the integration of cell cycle progression with cell size, which ensures robust cellular replication across many conditions.

Our observations are unlikely to be a peculiarity of *E. coli*. *B. subtilis* has also been shown to initiate DNA replication at a constant cell volume per *ori* at the population level.[53] Furthermore, this Gram-positive bacterium has been reported to display a constant ratio of FtsZ rings to cell length across four different growth rates.[73] This is consistent with a mean cell length threshold for FtsZ ring formation, suggesting that unifying rules in cell cycle control may be common.

Population vs. single-cell principles

It is important to note that the proposed cell cycle laws consist of population-level principles obtained by averaging the behavior of many individual cells. As such, they reflect what *E. coli* has evolved to do on average as a system. At the single-cell level, these governing principles could be achieved in different ways.[72,74,75] For example, the constant average cell volume per *ori* at DNA replication initiation, which is observed at the population level, can theoretically be obtained either by a "sizer" at the single-cell level, where individual cells initiate DNA replication at a constant volume per *ori*, or by an "adder," where individual cells add, on average, a constant volume per *ori* between consecutive DNA replication initiation events.[76] Time-lapse experiments have verified the adder scenario.[19,77]

Ultimately, combining knowledge from population and single-cell studies will be critical when searching for the biophysical mechanisms that underlie the cell cycle laws. In some cases, like the initiation of DNA replication at a constant cell volume per *ori*, there are theoretical and experimental clues pointing to potential cell size-dependent mechanisms.[19,78–81] In the case of FtsZ ring formation, the presence of a FtsZ ring over the nucleoid in most (36/41) tested media (Figures 5B–5D) precludes a predominant role for nucleoid occlusion in controlling FtsZ ring assembly. At the same time, nucleoid occlusion could still be relevant for FtsZ ring constriction, i.e., cell constriction.[82,83] Nucleoid and cell constriction almost coincide in nutrient-poor conditions (Figure S5A). However, this is not the case in rich conditions where nucleoids segregate well before initiation of cell division in rich media (Figure S5A). Therefore, we favor the idea of nucleoid occlusion acting as a failsafe mechanism that prevents cell constriction from initiating over (unconstricted) nucleoids rather than a trigger, as something else is clearly responsible for triggering cell constriction in nutrient-rich conditions.

In fact, the Min system alone may be sufficient to establish the two-rule principle regulating FtsZ ring formation: one ring per division cycle and the cell length threshold (Figures S7B and S7C). This system, which includes the FtsZ polymerization inhibitor MinC,[84] has been extensively studied for its role in FtsZ ring positioning along the cell length.[85,86] In the absence of MinC, bacterial cells form minicells and filaments due to the division septum forming near the cell poles.[87,88] Consistent with the role of the Min system in constraining FtsZ to a single ring per cell, we observed cells with multiple FtsZ rings in the *E. coli* Δ*minC* mutant strain throughout all sampled nutrient conditions (Figure S7B). In addition, this strain already formed (polar) FtsZ rings in small cells, at sizes considerably smaller than the length threshold below which no FtsZ rings were observed in the parent strain (Figure S7C). Also, by tracking individual cells during growth, we showed in previous work that the oscillation amplitude of MinD (the partner protein of the FtsZ polymerization inhibitor MinC) depends on cell length.[89] In fact, the cell length threshold at which we observed FtsZ ring formation in this current study (~2.8 μm) falls within the length interval (2–3 μm) in which depletion of MinD/C (and thus the minimum of FtsZ inhibition at midcell) first became apparent in our previous work.[89] As for the generational constraint of FtsZ ring formation, it may emerge from the fact that the oscillation of MinD/C only produces multiple minima in long ($\gtrsim$9 μm) cells.[90,91]

We did not find evidence of constant time delays between cell cycle events across strains and media, with the notable exception of the constant average time between cell constriction initiation and cell separation (Figure 6F). By analyzing the data from another study[54] that was performed at a lower temperature (28°C), we also found a constant average time of cell constriction across various nutrient conditions (Figures S6C and S6D), but interestingly, this average time was about twice longer than what we found at a higher temperature (37°C). A simple explanation for the constant time could be that it reflects the time it takes for the biochemical process of cell constriction to occur at that temperature. However, given that cells are wider in richer media, a constant time for cell constriction implies that wider cells constrict faster, as shown in Figure S6E. Consistent with this relationship, the cell constriction time has been shown to remain constant across a panel of MreB point mutants with varying cell widths.[92]

The proposed cell cycle laws provide both benchmarks and constraints for testing current and future mechanistic models of cell cycle control. Furthermore, for each cell cycle law, our study identified gene deletion outliers (Figure 7; Dataset S2), with the nutrient-independent ones being of particular interest. Some outliers do not break the rule per se; they only shift the constancy to a lower or higher set value (Figure 7D). Although this underscores the importance of a constant value across conditions, it also renders the proteins missing in these mutant strains unlikely to be involved in mechanisms underpinning the laws. These outliers remain, however, valuable tools for testing hypotheses because they provide a high level of constraint, as any proposed mechanism should display the expected shift in control set points in these mutant strains. Our study also identified outliers for which the rule of constancy no longer applied (Figure 7D; Dataset S2). In these mutants, the mechanism involved in a cell cycle law is likely broken, opening the door for future mechanistic studies.

Some nutrient-independent outliers for the proposed cell cycle laws broke more than one law (Figure 7; Dataset S2). For example, we identified several *tol* mutants as consistent outliers for all five governing principles (Figure 7C; Dataset S2). TolQ, TolR, and TolA are inner membrane components of the

Tol-Pal system, which spans the entire cell envelope.[93] The Tol-Pal system is known to be involved in outer membrane invagination, septal peptidoglycan processing, and maintenance of outer membrane integrity.[94–98] A recent study identified *tol* mutants that initiated DNA replication at smaller cell volumes than the wild type,[99] which we confirmed (Figure 7C). Our study shows that gene deletions of individual Tol components can also lead to severe phenotypes related to the timing of FtsZ ring formation, cell constriction, nucleoid segregation, and completion of cell division (Figure 7C; Dataset S2). The pleiotropic phenotypes of these deletion mutants (Figure S7D) suggest that this system could play a major role in integrating the DNA and division cycles.

The carbon source often drives mutant cell morphology and cell cycle phenotypes

Although the motivation of our study was to test previously proposed relations and uncover population-level principles of cell cycle regulation, our large dataset also allowed us to explore the phenotypic landscape of *E. coli* in more depth. We previously found that a large fraction (~20%) of the non-essential *E. coli* genome directly or indirectly affects cell morphology and/or cell cycle characteristics in a single growth condition.[35] Here, by varying the carbon sources, we showed that phenotypes usually depend on the nature of the nutrient available in the environment, as a severe ($|s| \geq 3$) phenotype in one condition was often not persistent across other nutrient conditions (Figures 7A and 7B). This indicates that central metabolism, which is dictated by nutrient availability, is the primary driver of phenotypes. Consistent with this idea, deletion mutants of central carbon metabolism exhibit diverse cell morphological alterations.[100] There are also practical implications of a metabolic dependence. Cell size or cell cycle mutants are often characterized under a single nutrient condition with the implicit assumption that the phenotypes would persist in most other conditions. Our work suggests that mutants may need to be examined through the lens of the metabolism that the cells experience.

Evolutionary implications

The large variability in phenotypes covered in our screen (Figure S2A) illustrates the broad range of the phenotypic space available to *E. coli*. Consider, for example, cell volume or the relative timing of DNA replication initiation. Across the tested nutrient conditions, over 200 deletion strains (i.e., almost a quarter of the examined deletion strains) differed by three or more SDs from the parent. However, by and large, mutants follow all five proposed cell cycle laws (Figures 2H, 4B, 5E, 5F, 6E, and 6F), including those related to cell size or DNA replication. Thus, the phenotypic variability in cell size, shape, and cell cycle timings contrasts with the robustness of the proposed cell cycle laws across genetic and metabolic perturbations. This suggests that the cell cycle laws are under strong evolutionary constraints while cell morphology can more rapidly evolve, explaining the rapid emergence of strains of the same species that vary substantially in cell shape and size.[101] The cell cycle laws provide a simple way to ensure faithful cell cycle progression by connecting cell cycle events to an aspect of cell size, even if cell morphology changes through mutations.

Reducing biological complexity to simple principles

It is important to note that we extensively analyzed our dataset to examine all kinds of possible relationships between the 77 features we measured. Only one governing principle emerged for each of the five cell cycle events, highlighting the discriminating aspect of our approach. In the literature, the bacterial cell cycle is often discussed in the context of two regimes: discrete vs. overlapping DNA replication cycles (slow vs. fast growth). Our findings suggest that this distinction may not be critical, as the proposed cell cycle laws apply, regardless of whether DNA replication cycles are discrete or overlapping. In fact, by plotting the relative timing of different cell cycle events versus the population doubling time, it is indeed possible to observe a distinct trend between slow and fast growth regimes (Figure S4C). However, our study demonstrates that this distinction disappears when the evaluation happens against a specific variable. This is when such unifying principles, which hold across diverse perturbations, can be identified.

Our approach also highlights the importance of using a large number of diverse perturbations to confidently identify governing principles. In our case, this enabled the uncoupling of cellular features that might otherwise appear to be dependent on each other, such as cell length and width (Figures 2B–2D) or growth rate and cell volume (Figures 2F and 2G). Using large-scale genetic perturbations achieves this effect by offering discriminating power, as it averages out the specific effect associated with each perturbation and increases confidence in any identified dependencies.[35–38] The cell cycle laws, together with the general growth law, provide simple and robust means of coordinating cell cycle progression with cell size and growth rate across various conditions. Thus, there appears to be an inherent robustness in the population-level design of cell cycle regulation, where even complex phenotypes can be deconstructed into a combination of simple but shared principles.

Our approach of simultaneously quantifying multiple features across a large collection of mutants under several nutrient conditions should be broadly applicable to the study of other aspects of bacterial physiology. Simple general principles may exist for other cellular processes such as gene expression, cell wall synthesis, metabolism, energy production/homeostasis, or second messenger production. Many of these processes can be tracked intracellularly through different fluorescent-labeling approaches or metabolic biosensors.[102–104] These tools, together with transposon or CRISPR interference libraries, open the door for similar large-scale, microscopy-based studies in a wide variety of species. Such an approach may reveal universal principles of cellular replication and physiology.

STAR★METHODS

Detailed methods are provided in the online version of this paper and include the following:

- KEY RESOURCES TABLE
- RESOURCE AVAILABILITY
  - Lead contact
  - Materials availability
  - Data and code availability
- EXPERIMENTAL MODEL AND SUBJECT DETAILS

SUPPLEMENTAL INFORMATION

Supplemental information can be found online at https://doi.org/10.1016/j.cels.2023.12.001.

ACKNOWLEDGMENTS

We thank Dr. Harold Erickson for sharing the FtsZ sandwich fusion used in this work and Dr. Suckjoon Jun for providing strain SJ_XTL229. We would also like to thank the Jacobs-Wagner laboratory for fruitful discussions and critical reading of the manuscript and specifically Jarno Mäkelä for providing the images of FtsZ-depleted cells. We also thank the members of the Govers laboratory for feedback on the manuscript. We would also like to thank Dr. Xiongfeng Dai for sharing their data on the DNA replication initiation volume. S.K.G. was partly funded by postdoctoral fellowships from the Belgian American Educational Foundation, Belgium (B.A.E.F.), the de Duve Institute, Belgium, and the F.R.S.-FNRS, Belgium; by a start-up grant (STG/21/068) from the KU Leuven Research Fund; and by the European Union (ERC Starting Grant BacterialBlueprint 101040800). C.J.-W. is an investigator of the Howard Hughes Medical Institute.

AUTHOR CONTRIBUTIONS

Conceptualization, S.K.G., M.C., and C.J.-W.; methodology, S.K.G., M.C., and C.J.-W.; software, S.K.G. and M.C.; formal analysis, S.K.G.; investigation, S.K.G. and B.T.; data curation, S.K.G..; writing – original draft, S.K.G. and C.J.-W.; writing – review & editing, S.K.G., M.C., G.L., and C.J.-W; visualization, S.K.G. and C.J.-W.; supervision, C.J.-W.; project administration, C.J.-W.; funding acquisition, C.J.-W.

DECLARATION OF INTERESTS

The authors declare no competing interests.

Received: January 12, 2023
Revised: June 15, 2023
Accepted: December 1, 2023
Published: December 28, 2023

REFERENCES

1. Surovtsev, I.V., and Jacobs-Wagner, C. (2018). Subcellular organization: a critical feature of bacterial cell replication. Cell *172*, 1271–1293.
2. Hochegger, H., Takeda, S., and Hunt, T. (2008). Cyclin-dependent kinases and cell-cycle transitions: does one fit all? Nat. Rev. Mol. Cell Biol. *9*, 910–916.
3. Vellai, T., and Vida, G. (1999). The origin of eukaryotes: the difference between prokaryotic and eukaryotic cells. Proc. Biol. Sci. *266*, 1571–1577.
4. Saxton, R.A., and Sabatini, D.M. (2017). mTOR Signaling in growth, metabolism, and disease. Cell *169*, 361–371.
5. Pierucci, O. (1978). Dimensions of Escherichia coli at various growth rates: model for envelope growth. J. Bacteriol. *135*, 559–574.
6. Schaechter, M., Maaloe, O., and Kjeldgaard, N.O. (1958). Dependency on medium and temperature of cell size and chemical composition during balanced grown of Salmonella typhimurium. J. Gen. Microbiol. *19*, 592–606.
7. Sargent, M.G. (1975). Control of cell length in Bacillus subtilis. J. Bacteriol. *123*, 7–19.
8. Cooper, S., and Helmstetter, C.E. (1968). Chromosome replication and the division cycle of Escherichia coli B/r. J. Mol. Biol. *31*, 519–540.
9. Donachie, W.D. (1968). Relationship between cell size and time of initiation of DNA replication. Nature *219*, 1077–1079.
10. Skarstad, K., Steen, H.B., and Boye, E. (1983). Cell cycle parameters of slowly growing Escherichia coli B/r studied by flow cytometry. J. Bacteriol. *154*, 656–662.
11. Bipatnath, M., Dennis, P.P., and Bremer, H. (1998). Initiation and velocity of chromosome replication in Escherichia coli B/r and K-12. J. Bacteriol. *180*, 265–273.
12. Michelsen, O., Teixeira de Mattos, M.J., Jensen, P.R., and Hansen, F.G. (2003). Precise determinations of C and D periods by flow cytometry in Escherichia coli K-12 and B/r. Microbiology (Reading) *149*, 1001–1010.
13. Wallden, M., Fange, D., Lundius, E.G., Baltekin, Ö., and Elf, J. (2016). The synchronization of replication and division cycles in individual E. coli cells. Cell *166*, 729–739.
14. Si, F., Li, D., Cox, S.E., Sauls, J.T., Azizi, O., Sou, C., Schwartz, A.B., Erickstad, M.J., Jun, Y., Li, X., et al. (2017). Invariance of initiation mass and predictability of cell size in Escherichia coli. Curr. Biol. *27*, 1278–1287.
15. Zheng, H., Ho, P.Y., Jiang, M., Tang, B., Liu, W., Li, D., Yu, X., Kleckner, N.E., Amir, A., and Liu, C. (2016). Interrogating the Escherichia coli cell cycle by cell dimension perturbations. Proc. Natl. Acad. Sci. USA *113*, 15000–15005.
16. Koppes, L.J., Meyer, M., Oonk, H.B., de Jong, M.A., and Nanninga, N. (1980). Correlation between size and age at different events in the cell division cycle of Escherichia coli. J. Bacteriol. *143*, 1241–1252.
17. Boye, E., Stokke, T., Kleckner, N., and Skarstad, K. (1996). Coordinating DNA replication initiation with cell growth: differential roles for DnaA and SeqA proteins. Proc. Natl. Acad. Sci. USA *93*, 12206–12211.
18. Hill, N.S., Kadoya, R., Chattoraj, D.K., and Levin, P.A. (2012). Cell size and the initiation of DNA replication in bacteria. PLoS Genet. *8*, e1002549.
19. Si, F., Le Treut, G., Sauls, J.T., Vadia, S., Levin, P.A., and Jun, S. (2019). Mechanistic origin of cell-size control and homeostasis in bacteria. Curr. Biol. *29*, 1760–1770.e7.
20. Wold, S., Skarstad, K., Steen, H.B., Stokke, T., and Boye, E. (1994). The initiation mass for DNA replication in Escherichia coli K-12 is dependent on growth rate. EMBO J. *13*, 2097–2102.
21. Churchward, G., Estiva, E., and Bremer, H. (1981). Growth rate-dependent control of chromosome replication initiation in Escherichia coli. J. Bacteriol. *145*, 1232–1238.
22. Zheng, H., Bai, Y., Jiang, M., Tokuyasu, T.A., Huang, X., Zhong, F., Wu, Y., Fu, X., Kleckner, N., Hwa, T., et al. (2020). General quantitative relations linking cell growth and the cell cycle in Escherichia coli. Nat. Microbiol. *5*, 995–1001.

23. Helmstetter, C.E. (1974). Initiation of chromosome replication in Escherichia coli. II. Analysis of the control mechanism. J. Mol. Biol. *84*, 21–36.

24. Zaritsky, A., and Zabrovitz, S. (1981). DNA synthesis in Escherichia coli during a nutritional shift-up. Mol. Gen. Genet. *181*, 564–566.

25. Bates, D., and Kleckner, N. (2005). Chromosome and replisome dynamics in E. coli: loss of sister cohesion triggers global chromosome movement and mediates chromosome segregation. Cell *121*, 899–911.

26. Moore, D.A., Whatley, Z.N., Joshi, C.P., Osawa, M., and Erickson, H.P. (2017). Probing for binding regions of the FtsZ protein surface through site-directed insertions: discovery of fully functional FtsZ-fluorescent proteins. J. Bacteriol. *199*, e00553-16.

27. Molina, F., and Skarstad, K. (2004). Replication fork and SeqA focus distributions in Escherichia coli suggest a replication hyperstructure dependent on nucleotide metabolism. Mol. Microbiol. *52*, 1597–1612.

28. Powell, E.O. (1956). Growth rate and generation time of bacteria, with special reference to continuous culture. J. Gen. Microbiol. *15*, 492–511.

29. Collins, J.F., and Richmond, M.H. (1962). Rate of growth of Bacillus cereus between divisions. J. Gen. Microbiol. *28*, 15–33.

30. Vischer, N.O., Verheul, J., Postma, M., van den Berg van Saparoea, B., Galli, E., Natale, P., Gerdes, K., Luirink, J., Vollmer, W., Vicente, M., et al. (2015). Cell age dependent concentration of Escherichia coli divisome proteins analyzed with ImageJ and ObjectJ. Front. Microbiol. *6*, 586.

31. Kafri, R., Levy, J., Ginzberg, M.B., Oh, S., Lahav, G., and Kirschner, M.W. (2013). Dynamics extracted from fixed cells reveal feedback linking cell growth to cell cycle. Nature *494*, 480–483.

32. Mangiameli, S.M., Veit, B.T., Merrikh, H., and Wiggins, P.A. (2017). The replisomes remain spatially proximal throughout the cell cycle in bacteria. PLoS Genet. *13*, e1006582.

33. Trojanowski, D., Ginda, K., Pióro, M., Hołówka, J., Skut, P., Jakimowicz, D., and Zakrzewska-Czerwińska, J. (2015). Choreography of the Mycobacterium replication machinery during the cell cycle. mBio *6*. e02125–e02114.

34. Reyes-Lamothe, R., Possoz, C., Danilova, O., and Sherratt, D.J. (2008). Independent positioning and action of Escherichia coli replisomes in live cells. Cell *133*, 90–102.

35. Campos, M., Govers, S.K., Irnov, I., Dobihal, G.S., Cornet, F., and Jacobs-Wagner, C. (2018). Genomewide phenotypic analysis of growth, cell morphogenesis, and cell cycle events in Escherichia coli. Mol. Syst. Biol. *14*, e7573.

36. Sachs, K., Perez, O., Pe'er, D., Lauffenburger, D.A., and Nolan, G.P. (2005). Causal protein-signaling networks derived from multiparameter single-cell data. Science *308*, 523–529.

37. Collinet, C., Stöter, M., Bradshaw, C.R., Samusik, N., Rink, J.C., Kenski, D., Habermann, B., Buchholz, F., Henschel, R., Mueller, M.S., et al. (2010). Systems survey of endocytosis by multiparametric image analysis. Nature *464*, 243–249.

38. Liberali, P., Snijder, B., and Pelkmans, L. (2015). Single-cell and multivariate approaches in genetic perturbation screens. Nat. Rev. Genet. *16*, 18–32.

39. Taheri-Araghi, S., Bradde, S., Sauls, J.T., Hill, N.S., Levin, P.A., Paulsson, J., Vergassola, M., and Jun, S. (2015). Cell-size control and homeostasis in bacteria. Curr. Biol. *25*, 385–391.

40. Campos, M., Surovtsev, I.V., Kato, S., Paintdakhi, A., Beltran, B., Ebmeier, S.E., and Jacobs-Wagner, C. (2014). A constant size extension drives bacterial cell size homeostasis. Cell *159*, 1433–1446.

41. Schmoller, K.M., Turner, J.J., Kõivomägi, M., and Skotheim, J.M. (2015). Dilution of the cell cycle inhibitor Whi5 controls budding-yeast cell size. Nature *526*, 268–272.

42. Facchetti, G., Knapp, B., Flor-Parra, I., Chang, F., and Howard, M. (2019). Reprogramming Cdr2-dependent geometry-based cell size control in fission yeast. Curr. Biol. *29*, 350–358.e4.

43. Harris, L.K., and Theriot, J.A. (2018). Surface area to volume ratio: a natural variable for bacterial morphogenesis. Trends Microbiol. *26*, 815–832.

44. Shi, H., Hu, Y., Odermatt, P.D., Gonzalez, C.G., Zhang, L., Elias, J.E., Chang, F., and Huang, K.C. (2021). Precise regulation of the relative rates of surface area and volume synthesis in bacterial cells growing in dynamic environments. Nat. Commun. *12*, 1975.

45. Harris, L.K., Dye, N.A., and Theriot, J.A. (2014). A Caulobacter MreB mutant with irregular cell shape exhibits compensatory widening to maintain a preferred surface area to volume ratio. Mol. Microbiol.

46. Ojkic, N., Serbanescu, D., and Banerjee, S. (2019). Surface-to-volume scaling and aspect ratio preservation in rod-shaped bacteria. eLife *8*, e47033.

47. Shi, H., Colavin, A., Bigos, M., Tropini, C., Monds, R.D., and Huang, K.C. (2017). Deep phenotypic mapping of bacterial cytoskeletal mutants reveals physiological robustness to cell size. Curr. Biol. *27*, 3419–3429.e4.

48. Vadia, S., Tse, J.L., Lucena, R., Yang, Z., Kellogg, D.R., Wang, J.D., and Levin, P.A. (2017). Fatty acid availability sets cell envelope capacity and dictates microbial cell size. Curr. Biol. *27*, 1757–1767.e5.

49. Gray, W.T., Govers, S.K., Xiang, Y., Parry, B.R., Campos, M., Kim, S., and Jacobs-Wagner, C. (2019). Nucleoid size scaling and intracellular organization of translation across bacteria. Cell *177*, 1632–1648.e20.

50. Wu, F., Swain, P., Kuijpers, L., Zheng, X., Felter, K., Guurink, M., Solari, J., Jun, S., Shimizu, T.S., Chaudhuri, D., et al. (2019). Cell boundary confinement sets the size and position of the E. coli chromosome. Curr. Biol. *29*, 2131–2144.e4.

51. Dai, X., and Zhu, M. (2018). High osmolarity modulates bacterial cell size through reducing initiation volume in Escherichia coli. mSphere *3*, e00430-18.

52. Zhu, M., Dai, X., Guo, W., Ge, Z., Yang, M., Wang, H., and Wang, Y.P. (2017). Manipulating the bacterial cell cycle and cell size by titrating the expression of ribonucleotide reductase. mBio *8*, e01741-17.

53. Sauls, J.T., Cox, S.E., Do, Q., Castillo, V., Ghulam-Jelani, Z., and Jun, S. (2019). Control of Bacillus subtilis replication initiation during physiological transitions and perturbations. mBio *10*, e02205-19.

54. Tiruvadi-Krishnan, S., Männik, J., Kar, P., Lin, J., Amir, A., and Männik, J. (2022). Coupling between DNA replication, segregation, and the onset of constriction in Escherichia coli. Cell Rep. *38*, 110539.

55. Mercier, R., Petit, M.A., Schbath, S., Robin, S., El Karoui, M., Boccard, F., and Espéli, O. (2008). The MatP/matS site-specific system organizes the terminus region of the E. coli chromosome into a macrodomain. Cell *135*, 475–485.

56. Walker, B.E., Männik, J., and Männik, J. (2020). Transient membrane-linked FtsZ assemblies precede Z-ring formation in Escherichia coli. Curr. Biol. *30*, 499–508.e6.

57. Männik, J., Walker, B.E., and Männik, J. (2018). Cell cycle-dependent regulation of FtsZ in Escherichia coli in slow growth conditions. Mol. Microbiol. *110*, 1030–1044.

58. Den Blaauwen, T., Buddelmeijer, N., Aarsman, M.E., Hameete, C.M., and Nanninga, N. (1999). Timing of FtsZ assembly in Escherichia coli. J. Bacteriol. *181*, 5167–5175.

59. Coltharp, C., Buss, J., Plumer, T.M., and Xiao, J. (2016). Defining the rate-limiting processes of bacterial cytokinesis. Proc. Natl. Acad. Sci. USA *113*, E1044–E1053.

60. Hocking, J., Priyadarshini, R., Takacs, C.N., Costa, T., Dye, N.A., Shapiro, L., Vollmer, W., and Jacobs-Wagner, C. (2012). Osmolality-dependent relocation of penicillin-binding protein PBP2 to the division site in Caulobacter crescentus. J. Bacteriol. *194*, 3116–3127.

61. Levin, P.A., and Janakiraman, A. (2021). Localization, assembly, and activation of the Escherichia coli cell division machinery. EcoSal Plus *9*. eESP00222021.

62. Wu, L.J., and Errington, J. (2011). Nucleoid occlusion and bacterial cell division. Nat. Rev. Microbiol. *10*, 8–12.

63. Bernhardt, T.G., and de Boer, P.A. (2005). SlmA, a nucleoid-associated, FtsZ binding protein required for blocking septal ring assembly over chromosomes in E. coli. Mol. Cell *18*, 555–564.

64. Ortiz, C., Natale, P., Cueto, L., and Vicente, M. (2016). The keepers of the ring: regulators of FtsZ assembly. FEMS Microbiol. Rev. *40*, 57–67.

65. Adams, D.W., Wu, L.J., and Errington, J. (2014). Cell cycle regulation by the bacterial nucleoid. Curr. Opin. Microbiol. *22*, 94–101.

66. Männik, J., and Bailey, M.W. (2015). Spatial coordination between chromosomes and cell division proteins in Escherichia coli. Front. Microbiol. *6*, 306.

67. Wu, L.J., and Errington, J. (2004). Coordination of cell division and chromosome segregation by a nucleoid occlusion protein in Bacillus subtilis. Cell *117*, 915–925.

68. Adler, H.I., Fisher, W.D., Cohen, A., and Hardigree, A.A. (1967). Miniature Escherichia coli cells deficient in DNA. Proc. Natl. Acad. Sci. USA *57*, 321–326.

69. Camberg, J.L., Hoskins, J.R., and Wickner, S. (2009). ClpXP protease degrades the cytoskeletal protein, FtsZ, and modulates FtsZ polymer dynamics. Proc. Natl. Acad. Sci. USA *106*, 10614–10619.

70. LaBreck, C.J., Trebino, C.E., Ferreira, C.N., Morrison, J.J., DiBiasio, E.C., Conti, J., and Camberg, J.L. (2021). Degradation of MinD oscillator complexes by Escherichia coli ClpXP. J. Biol. Chem. *296*, 100162.

71. Donachie, W.D., and Begg, K.J. (1989). Cell length, nucleoid separation, and cell division of rod-shaped and spherical cells of Escherichia coli. J. Bacteriol. *171*, 4633–4639.

72. Kar, P., Tiruvadi-Krishnan, S., Männik, J., Männik, J., and Amir, A. (2023). Using conditional independence tests to elucidate causal links in cell cycle regulation in Escherichia coli. Proc. Natl. Acad. Sci. USA *120*, e2214796120.

73. Weart, R.B., Lee, A.H., Chien, A.C., Haeusser, D.P., Hill, N.S., and Levin, P.A. (2007). A metabolic sensor governing cell size in bacteria. Cell *130*, 335–347.

74. Joshi, K., Wright, C.S., Ziegler, K.F., Spiers, E.M., Crosser, J.T., Eschker, S., Biswas, R.R., and Iyer-Biswas, S. (2023). Emergent simplicities in stochastic intergenerational homeostasis. Preprint at bioRxiv. https://doi.org/10.1101/2023.01.18.524627.

75. Joshi, K., Biswas, R.R., and Iyer-Biswas, S. (2023). Intergenerational scaling law determines the precision kinematics of stochastic individual-cell-size homeostasis. Preprint at bioRxiv. https://doi.org/10.1101/2023.01.20.525000.

76. Ho, P.Y., and Amir, A. (2015). Simultaneous regulation of cell size and chromosome replication in bacteria. Front. Microbiol. *6*, 662.

77. Witz, G., van Nimwegen, E., and Julou, T. (2019). Initiation of chromosome replication controls both division and replication cycles in E. coli through a double-adder mechanism. eLife *8*, e48063.

78. Knöppel, A., Broström, O., Gras, K., Fange, D., and Elf, J. (2022). The coordination of replication initiation with growth rate in *Escherichia coli*. Preprint at bioRxiv.

79. Zhang, Q., Zhang, Z., and Shi, H. (2020). Cell size is coordinated with cell cycle by regulating initiator protein DnaA in E. coli. Biophys. J. *119*, 2537–2557.

80. Berger, M., and Wolde, P.R.T. (2022). Robust replication initiation from coupled homeostatic mechanisms. Nat. Commun. *13*, 6556.

81. Sompayrac, L., and Maaloe, O. (1973). Autorepressor model for control of DNA replication. Nat. New Biol. *241*, 133–135.

82. Mulder, E., and Woldringh, C.L. (1989). Actively replicating nucleoids influence positioning of division sites in Escherichia coli filaments forming cells lacking DNA. J. Bacteriol. *171*, 4303–4314.

83. Woldringh, C.L., Mulder, E., Valkenburg, J.A., Wientjes, F.B., Zaritsky, A., and Nanninga, N. (1990). Role of the nucleoid in the toporegulation of division. Res. Microbiol. *141*, 39–49.

84. Hu, Z., Mukherjee, A., Pichoff, S., and Lutkenhaus, J. (1999). The MinC component of the division site selection system in Escherichia coli interacts with FtsZ to prevent polymerization. Proc. Natl. Acad. Sci. USA *96*, 14819–14824.

85. Rowlett, V.W., and Margolin, W. (2015). The Min system and other nucleoid-independent regulators of Z ring positioning. Front. Microbiol. *6*, 478.

86. Ramm, B., Heermann, T., and Schwille, P. (2019). The E. coli MinCDE system in the regulation of protein patterns and gradients. Cell. Mol. Life Sci. *76*, 4245–4273.

87. de Boer, P.A.J., Crossley, R.E., and Rothfield, L.I. (1989). A division inhibitor and a topological specificity factor coded for by the minicell locus determine proper placement of the division septum in E. coli. Cell *56*, 641–649.

88. Levin, P.A., Shim, J.J., and Grossman, A.D. (1998). Effect of minCD on FtsZ ring position and polar septation in Bacillus subtilis. J. Bacteriol. *180*, 6048–6051.

89. Sliusarenko, O., Heinritz, J., Emonet, T., and Jacobs-Wagner, C. (2011). High-throughput, subpixel precision analysis of bacterial morphogenesis and intracellular spatio-temporal dynamics. Mol. Microbiol. *80*, 612–627.

90. MacCready, J.S., and Vecchiarelli, A.G. (2018). In long bacterial cells, the Min system can act off-center. Mol. Microbiol. *109*, 268–272.

91. Wehrens, M., Ershov, D., Rozendaal, R., Walker, N., Schultz, D., Kishony, R., Levin, P.A., and Tans, S.J. (2018). Size laws and division ring dynamics in filamentous Escherichia coli cells. Curr. Biol. *28*, 972–979.e5.

92. Sun, J., Shi, H., and Huang, K.C. (2021). Hyperosmotic shock transiently accelerates constriction rate in Escherichia coli. Front. Microbiol. *12*, 718600.

93. Egan, A.J.F. (2018). Bacterial outer membrane constriction. Mol. Microbiol. *107*, 676–687.

94. Cascales, E., Bernadac, A., Gavioli, M., Lazzaroni, J.C., and Lloubes, R. (2002). Pal lipoprotein of Escherichia coli plays a major role in outer membrane integrity. J. Bacteriol. *184*, 754–759.

95. Gerding, M.A., Ogata, Y., Pecora, N.D., Niki, H., and de Boer, P.A. (2007). The trans-envelope Tol-Pal complex is part of the cell division machinery and required for proper outer-membrane invagination during cell constriction in E. coli. Mol. Microbiol. *63*, 1008–1025.

96. Typas, A., Banzhaf, M., van den Berg van Saparoea, B., Verheul, J., Biboy, J., Nichols, R.J., Zietek, M., Beilharz, K., Kannenberg, K., von Rechenberg, M., et al. (2010). Regulation of peptidoglycan synthesis by outer-membrane proteins. Cell *143*, 1097–1109.

97. Yakhnina, A.A., and Bernhardt, T.G. (2020). The Tol-Pal system is required for peptidoglycan-cleaving enzymes to complete bacterial cell division. Proc. Natl. Acad. Sci. USA *117*, 6777–6783.

98. Hale, C.A., Persons, L., and de Boer, P.A.J. (2022). Recruitment of the TolA protein to cell constriction sites in Escherichia coli via three separate mechanisms, and a critical role for FtsWI activity in recruitment of both TolA and TolQ. J. Bacteriol. *204*, e0046421.

99. Camsund, D., Lawson, M.J., Larsson, J., Jones, D., Zikrin, S., Fange, D., and Elf, J. (2020). Time-resolved imaging-based CRISPRi screening. Nat. Methods *17*, 86–92.

100. Westfall, C.S., and Levin, P.A. (2018). Comprehensive analysis of central carbon metabolism illuminates connections between nutrient availability, growth rate, and cell morphology in Escherichia coli. PLoS Genet. *14*, e1007205.

101. Desmarais, S.M., Tropini, C., Miguel, A., Cava, F., Monds, R.D., de Pedro, M.A., and Huang, K.C. (2015). High-throughput, highly sensitive analyses of bacterial morphogenesis using ultra performance liquid chromatography. J. Biol. Chem. *290*, 31090–31100.

102. Sun, Z., Wu, R., Zhao, B., Zeinert, R., Chien, P., and You, M. (2021). Live-cell imaging of guanosine tetra- and pentaphosphate (p)ppGpp with RNA-based fluorescent sensors*. Angew. Chem. Int. Ed. Engl. *60*, 24070–24074.

103. Yaginuma, H., Kawai, S., Tabata, K.V., Tomiyama, K., Kakizuka, A., Komatsuzaki, T., Noji, H., and Imamura, H. (2014). Diversity in ATP

concentrations in a single bacterial cell population revealed by quantitative single-cell imaging. Sci. Rep. *4*, 6522.

104. Kaczmarczyk, A., van Vliet, S., Jakob, R.P., Reinders, A., Klotz, A., Maier, T., and Jenal, U. (2022). A novel biosensor reveals dynamic changes of C-di-GMP in differentiating cells with ultra-high temporal resolution. Preprint at bioRxiv. https://doi.org/10.1101/2022.10.18.512705.

105. Guyer, M.S., Reed, R.R., Steitz, J.A., and Low, K.B. (1981). Identification of a sex-factor-affinity site in E. coli as gamma delta. Cold Spring Harb. Symp. Quant. Biol. *45*, 135–140.

106. Li, X.T., Jun, Y., Erickstad, M.J., Brown, S.D., Parks, A., Court, D.L., and Jun, S. (2016). tCRISPRi: tunable and reversible, one-step control of gene expression. Sci. Rep. *6*, 39076.

107. Collins, T.J. (2007). ImageJ for microscopy. BioTechniques *43* (*Suppl*), 25–30.

108. Paintdakhi, A., Parry, B., Campos, M., Irnov, I., Elf, J., Surovtsev, I., and Jacobs-Wagner, C. (2016). Oufti: an integrated software package for high-accuracy, high-throughput quantitative microscopy analysis. Mol. Microbiol. *99*, 767–777.

109. Baba, T., Ara, T., Hasegawa, M., Takai, Y., Okumura, Y., Baba, M., Datsenko, K.A., Tomita, M., Wanner, B.L., and Mori, H. (2006). Construction of Escherichia coli K-12 in-frame, single-gene knockout mutants: the Keio collection. Mol. Syst. Biol. *2*, 2006.0008.

110. Datsenko, K.A., and Wanner, B.L. (2000). One-step inactivation of chromosomal genes in Escherichia coli K-12 using PCR products. Proc. Natl. Acad. Sci. USA *97*, 6640–6645.

111. Yang, X., Lyu, Z., Miguel, A., McQuillen, R., Huang, K.C., and Xiao, J. (2017). GTPase activity-coupled treadmilling of the bacterial tubulin FtsZ organizes septal cell wall synthesis. Science *355*, 744–747.

112. Adiciptaningrum, A., Osella, M., Moolman, M.C., Cosentino Lagomarsino, M., and Tans, S.J. (2015). Stochasticity and homeostasis in the E. coli replication and division cycle. Sci. Rep. *5*, 18261.

113. Männik, J., Pichoff, S., Lutkenhaus, J., and Männik, J. (2022). Cell cycle-dependent recruitment of FtsN to the divisome in Escherichia coli. mBio *13*, e0201722.

114. Weiss, D.S. (2015). Last but not least: new insights into how FtsN triggers constriction during Escherichia coli cell division. Mol. Microbiol. *95*, 903–909.

115. Liu, B., Persons, L., Lee, L., and de Boer, P.A. (2015). Roles for both FtsA and the FtsBLQ subcomplex in FtsN-stimulated cell constriction in Escherichia coli. Mol. Microbiol. *95*, 945–970.

116. Boes, A., Olatunji, S., Breukink, E., and Terrak, M. (2019). Regulation of the peptidoglycan polymerase activity of PBP1b by antagonist actions of the core divisome proteins FtsBLQ and FtsN. mBio *10*, e01912–e01918.

117. Herendeen, S.L., VanBogelen, R.A., and Neidhardt, F.C. (1979). Levels of major proteins of Escherichia coli during growth at different temperatures. J. Bacteriol. *139*, 185–194.

118. Colin, A., Micali, G., Faure, L., Cosentino Lagomarsino, M., and van Teeffelen, S. (2021). Two different cell-cycle processes determine the timing of cell division in Escherichia coli. eLife *10*, e67495.

119. Atolia, E., Cesar, S., Arjes, H.A., Rajendram, M., Shi, H., Knapp, B.D., Khare, S., Aranda-Díaz, A., Lenski, R.E., and Huang, K.C. (2020). Environmental and physiological factors affecting high-throughput measurements of bacterial growth. mBio *11*, e01378-20.

120. Zwietering, M.H., Jongenburger, I., Rombouts, F.M., and van 'T Riet, K. (1990). Modeling of the bacterial growth curve. Appl. Environ. Microbiol. *56*, 1875–1881.

STAR★METHODS

KEY RESOURCES TABLE

REAGENT or RESOURCE	SOURCE	IDENTIFIER
Bacterial and virus strains		
E. coli MG1655	Guyer et al.[105]	N/A
E. coli MG1655 *seqA*::*seqA-mcherry ftsZ*::*ftsZ-venus*^{SW}	Gray et al.[49]	CJW6324
Individual deletion mutants in *E. coli* MG1655 *seqA*::*seqA-mcherry ftsZ*::*ftsZ-venus*^{SW}	This paper	See Dataset S2
E. coli ftsZ CRISPRi strain	Li et al.[106]	SJ_XTL229
Chemicals, peptides, and recombinant proteins		
Agarose	AmericanBio	Cat#AB00972-00500
4',6-Diamidine-2′-phenylindole dihydrochloride (DAPI) fluorescent dye	Thermo Fisher Scientific	Cat#D1306
Phusion high-fidelity polymerase	New England Biolabs	Cat#M0530S
LB	Fisher Scientific	Cat#BP1426-2
BHI	Fisher Scientific	Cat#11469668
NB	Fisher Scientific	Cat#10679125
TSB	Fisher Scientific	Cat#10098983
Oligonucleotides		
Primers for strain verification/construction	This paper, Integrated DNA Technologies	See Table S3
Software and algorithms		
ImageJ	Collins[107]	https://imagej.nih.gov/ij/
MATLAB	Mathworks	https://www.mathworks.com/
Oufti	Paintdakhi et al.[108]	https://oufti.org/
Github code repository of the Jacobs-Wagner lab		https://doi.org/10.5281/zenodo.10139532

RESOURCE AVAILABILITY

Lead contact

Further information and requests for resources and reagents should be directed to and will be fulfilled by the lead contact, Christine Jacobs-Wagner (jacobs-wagner@stanford.edu).

Materials availability

All bacterial strains generated in this study are available from the lead contact.

Data and code availability

All datasets used in this manuscript are available in the supplemental information (Dataset S1 and S2) and were deposited at GitHub, where they are publicly available as of the date of publication. DOI is listed in the key resources table. Microscopy data reported in this paper will be shared by Dr. Sander Govers upon reasonable request. All original code developed as part of this study has been deposited at GitHub and is publicly available as of the date of publication. DOI is listed in the key resources table. Any additional information required to reanalyze the data reported in this paper is available from the lead contact upon request.

EXPERIMENTAL MODEL AND SUBJECT DETAILS

Bacterial strains

Strain CJW6324 (MG1655 *seqA*::*seqA-mcherry ftsZ*::*ftsZ-venus*^{SW})[49] was used as the parent strain throughout this study. Individual deletions (n = 806) were moved into the parent strain by P1 phage transduction to assemble a deletion strain library. To do this, lysates were prepared from the corresponding deletion strains of the *E. coli* Keio collection.[109] Strains for which the transduction failed were constructed using lambda red recombineering.[110] After initial construction of the library, 115 deletion strains were randomly chosen and verified by colony PCR (primers are listed in Table S3). The small fraction (< 5%) of incorrect deletion strains identified by colony PCR were reconstructed using lambda red recombineering. While the FtsZ-Venus^{SW} fusion is known to cause a mild cell

elongation phenotype particularly in nutrient-rich conditions,[26,111] it can support cell division as the sole source of FtsZ within a cell, and does so across all deletion strains included in this study. Any potential artefact of the fluorescent fusions used in this study is also mitigated by the fact that all strains are equipped with them, thereby enabling a relative comparison.

Individual gene deletion strains (806) were selected using a previous genome-wide, image-based quantitative screen of the Keio *E. coli* single-gene deletion collection grown in M9gluCAAT.[35] Among the 806 strains imaged in our study, 93 of them were selected based on their phenotypes related to the positive correlation between nucleoid size and cell size (nucleocytoplasmic ratio), and the negative correlation between nucleoid size and the relative timing of nucleoid separation.[35] These strains were identified as outliers ($|s|>3$) for these relationships by calculating their distance to a linear fit obtained by including all strains. These 93 strains were combined with 713 strains that clustered together in specific morphology islands (2, 3, 6, 7, 8, 9, 11, 12, 13, 14, 16, 17, 18, 19, 20, 21, 22) or cell cycle islands (2, 3, 4, 7, 8, 9, 11, 12) identified in our initial screen,[35] to obtain the final collection of 806 deletion strains. All islands contained strains with similar phenotypes, which significantly differed from the parent ($|s|>3$) in one or more morphological or cell cycle features. The selected islands contained strains that displayed deviations in more features than growth-related features alone (growth rate and OD_{max}), in order to avoid strains that only displayed growth defects. Genes were associated with clusters of orthologous groups (COGs) as in our previous work.[35]

METHOD DETAILS

Growth conditions

An overview of the 41 different nutrient conditions used in this study is provided in Table S1. Each strain was grown to stationary phase in the appropriate nutrient condition in pre-culture tubes (2 ml of growth media) in a shaking water bath at 37°C. A dilution (>1/10000) was then used to inoculate fresh growth medium (2 ml). The resulting cultures were allowed to grow until they reached an optical density at 600 nm (OD_{600}) between 0.05 and 0.3 depending on the nutrient condition (Figure S2C) before sampling for microscopy. The absence of strong biases in average feature behavior across this OD_{600} window (Figure S2C) suggests that most strains were sampled during steady-state exponential growth.

Microscopy

Cells were imaged on 1% agarose pads supplemented with either M9 buffer (for M9-based nutrient conditions) or the appropriate growth medium (for the richest, undefined nutrient conditions). To stain the chromosomal DNA that forms the nucleoid, cells were incubated with 1 μg/ml 4′,6-diamidino-2-phenylindole (DAPI) for 15 min in their growth medium prior to sampling for microscopy. To avoid having to correct for temporal biases introduced by cells spending longer times on agarose pads,[35] at most two deletion strains or parent replicates were spotted (0.5 μl) on the same pad. Separated spots were then traced back under the microscope and imaging was performed within 5-10 min after spotting the cells on the pad.

Phase contrast and epifluorescence imaging was performed on a Nikon Eclipse Ti microscope equipped with a 1.45 NA phase contrast CFI Plan Apo DM Lambda 100x oil objective (Nikon), an Orca-Flash4.0 V2 142 CMOS camera (Hamamatsu), and a Spectra X light engine (Lumencor). The following Chroma filter sets were used to acquire fluorescence images: DAPI (excitation ET350/50x, dichroic T400lp, emission ET460/50 m), YFP (excitation ET500/20x, dichroic T515lp, emission ET535/30 m) and mCherry/TexasRed (excitation ET560/40x, dichroic T585lpxr, emission ET630/75 m). The microscope was controlled by the NIS-Elements AR software.

Growth curves

Growth curves for the parent and deletion strains in various nutrient conditions were obtained in 96-well plates using a Synergy2 microplate reader (BioTek). Stationary phase precultures were inoculated into 150 μl fresh medium at a dilution of 1/300. Cultures were then grown for 60 h at 37°C during which OD_{600} measurements were taken every 4 min.

QUANTIFICATION AND STATISTICAL ANALYSIS

Image processing

Individual cells were detected using the open-source software package Oufti.[108] Cell contours were curated in an automated fashion using a trained support vector machine model[49] to automatically remove poor and incorrect cell detections. To avoid interference of neighboring cells, the support vector machine model was trained to remove cells that lie adjacent to other cells, as this can affect the extraction of cellular features. Cellular dimensions of retained cell contours were then quantified. Nucleoid outlines were detected using the objectDetection module in Oufti, from which nucleoid characteristics were extracted. The same parameters were used for all cell and nucleoid detections (see Tables S4 and S5 for the Oufti parameter values used in our study) to allow reliable comparison between strains and nutrient conditions. This is important, as the estimation of cellular features can vary with the chosen parameters.[49] In addition, we also set the parameters that constrain the fit of the final outline to negligible values, as in our previous work.[35] This avoids biasing the cell length or cell width estimate towards the initial guess value.

Note that a small consistent downshift of the added length value between birth and cell constriction initiation was observed in one nutrient condition (M9glu) relative to the other three conditions for both the parent and deletion strains (Figure 6E). This suggests the presence of a small systematic measurement error, though its origin is unknown.

The FtsZ-Venus^{SW} fusion provided information on the formation and position of the FtsZ ring,[26,57] whereas the SeqA-mCherry fusion allowed us to determine the DNA replication status of individual cells as well as the number of ongoing rounds of DNA replication.[13,27,112] FtsZ-Venus^{SW} and SeqA-mCherry signal information was added to Oufti-generated cell lists using the MATLAB functions Add_FtsZ_Characteristics.m and Add_SeqA_Characteristics.m, respectively.

Extraction of cellular characteristics

Properties of individual cells (cell and nucleoid dimensions, DAPI fluorescence intensity, fluorescent marker behavior, etc.) were extracted from Oufti cell lists using the MATLAB function Extract_Extended_Cell_Properties.m. Morphological features (e.g., cell length, area, and volume) were determined by summing the dimensions of each segment of the cell mesh identified by Oufti (assuming cylindrical shape for the cell volume). The cell or nucleoid width was calculated by taking the average of the widest 1/3rd of cell or nucleoid segments (thereby effectively excluding the cell or nucleoid pole regions and constricting septa). See https://oufti.org/ for more details. These features of individual cells were used to calculate 77 different population features for each strain in each nutrient condition (see Datasets S1 and S2).

Extraction of average relative timings of cell cycle events

To extract the relative timings of cell cycle events from exponentially growing populations, we relied on an established method that uses the proportions of cells at different cell cycle stages to infer the relative cell ages at which specific cell cycle events occur under steady-state conditions.[20,28,29] This method has been experimentally validated through comparison with time-lapse experiments by several groups.[31–34] In addition, for a previous study,[35] we performed a similar validation by comparing the relative timing of two cell cycle events (initiation of cell constriction and nucleoid separation), calculated using either time-lapse data or static images (i.e., randomly chosen frames from the same experiment). We found that the results from the time-lapse and static data were indeed in excellent agreement (see Figure on page 6 of the Peer Review Summary of our previous work,[35] which can be found at this weblink: https://www.embopress.org/action/downloadSupplement?doi=10.15252/msb.20177573&file=msb177573.reviewer_comments.pdf).

To calculate the relative timing of cell and nucleoid constriction, the fraction of unconstricted cells or nucleoids was determined using a "maximal signal profile indentation" threshold[89] of 0.2 μm (Figures S1B–S1D), typically corresponding to a constriction of 0.1 μm on either side of the cell or nucleoid. This threshold was chosen conservatively to exclude cells that had definitively committed to cell or nucleoid constriction. To validate this indentation threshold, we examined the maximal indentation of the phase contrast profiles of filamentous FtsZ-depleted cells (tCRISPRi, strain SJ_XTL229[106]), which provide a standard for unconstricted cells. For this validation, SJ_XTL229 cells were first grown in M9glyCAAT to steady-state exponential growth (at 37°C), after which 0.2% of L-arabinose was added to induce depletion of FtsZ. Cells were then sampled for microscopy 60 min later, a timepoint after which cell divisions were typically no longer observed. This analysis of non-constricting cells identified a 0.2 μm threshold as an appropriate threshold (Figure S1C), as anything lower would lead to incorrect assignments of cell constriction in non-constricting cell filaments. In addition, it confirmed our intuition that indentation slowly increases with cell sizes likely due to the probability of random variations increasing in larger cells. The maximal indentation of signal profiles (either phase contrast or DAPI) was measured in absolute length units to preclude cell width deviations from affecting the determination of constricting cells or nucleoids. This was achieved by multiplying relative cell or nucleoid indentation measurements (obtained by Oufti using integrated intensity profiles of individual cells[89,108]) by the cell or nucleoid width, respectively. We also compared results obtained from relative and absolute cell constriction measurements. They yielded a similar bilinear relationship between the maximal indentation of the phase contrast signal and the length of individual cells. However, only absolute cell constriction measurements led to invariance and unifying laws across the tested perturbations, and were thus retained throughout this study. For the relative timing of nucleoid separation, the fraction of cells with a single nucleoid was determined. For the relative timing of midcell FtsZ ring formation, the fraction of cells that did not display a clear FtsZ ring in the middle of the cell was determined using thresholds on the relative area and the relative midcell enrichment of the FtsZ-Venus^{SW} signal (Figure S1F). The midcell enrichment was assessed by comparing the FtsZ-Venus^{SW} signal in the middle 20% of a cell versus that in the remaining 80% of the cell.

To independently validate the cell cycle laws involving cell constriction and show that they are robust to the means by which cell constriction is identified, we took advantage of a recently published microfluidics study[54] by Tiruvadi-Krishnan et al. Their dataset contains information on the timing of cell constriction across different nutrient conditions.[54] In that study, initiation of cell constriction was determined in two ways that differed from our methodology: (i) by examining the increase of the phase contrast signal at midcell from kymographs and (ii) by determining the appearance of Ypet-FtsN at midcell from kymographs.[54] FtsN is the last known component of the divisome to assemble at midcell and its arrival has been reported to coincide with the initiation of cell constriction.[113–116] In line with our findings, our analysis of the data from this independent study showed that cell constriction occurs, on average, after the addition of a relatively constant cell length (Figure S6B). Compared to our data, the values for the added length from birth to constriction initiation differed due to differences in image analysis, but more importantly, the relative constancy across nutrient conditions remained. In addition to this first validation, we also observed a constant time between the initiation of cell constriction and its completion using the dataset by Tiruvadi-Krishnan et al.[54], independent on whether cell constriction was identified using the phase contrast or Ypet-FtsN signal (Figures S6D and S6E). The constriction times were longer than what we report, which was unsurprising given that an approximately 2-fold scaling factor is expected for growth rate differences between 28°C (their study) and 37°C (ours).[117]

All proposed cell cycle laws (i.e., constant nucleoid length at nucleoid constriction initiation, constant cell length added between birth and cell constriction initiation, constant constriction time, and constant cell length at FtsZ ring formation in poorer nutrient conditions) were robust to variations in the choice of threshold values (Figures S8 and S9). To examine whether potential cell length defects associated with the FtsZ-Venus^{SW} fusion[26] affect our conclusions of constancy, we imaged unlabeled wild-type cells and found that they displayed a constant mean nucleoid length at nucleoid constriction initiation (Figure S10A) and a constant mean added cell length at cell constriction initiation (Figure S10B).

Calculations of the relative timing of DNA replication initiation and termination relied on combining the SeqA-mCherry signal with cell volume measurements. In nutrient conditions in which cells displayed at least one clear period without ongoing DNA replication (as in M9Lala, M9gly, and M9glu media), as evidenced by a larger relative SeqA-mCherry area (Figure S1E, top row), distinct groups of cells could be identified (using k-means clustering), with each group corresponding to cells in a different DNA replication period. Depending on the DNA replication period, these cells differ in their number of origins (*ori*) and termini (*ter*) (Figure S1E). This information was used to calculate the average number of origins (<*ori*>) and termini (<*ter*>), which enabled the extraction of the relative duration of the C and D periods (Figure S1E).[14] The relative duration of the B period, which corresponds to the relative timing of DNA replication initiation, is given by B = 1 – (C+D). In richer nutrient conditions (e.g., M9LaraCAAT), cells continuously replicated their DNA, as evidenced by the consistently small relative SeqA-mCherry area (Figure S1E, bottom row). In these conditions, termination of DNA replication could not be determined as other rounds of DNA replication were still ongoing. However, DNA replication re-initiation events were identified by examining the relative position of the (brightest) SeqA-mCherry focus, which moved from midcell to a quarter cell position upon re-initiation (Figures 3C and S1E). In contrast to how it has occasionally been interpreted,[78,118] this re-localization did not appear to be preceded by a termination event, as cells without ongoing DNA replication could not be detected (based on the relative area of the SeqA-mCherry signal; Figure S1E) in these nutrient-rich conditions. The presence of overlapping rounds of DNA replication, where a new round initiates before the previous one has terminated, is also in line with what is known about chromosome replication in *E. coli* in richer growth conditions (supporting growth rates > ~1 h^{-1}).[8] Combining the information on SeqA-mCherry localization with cell volume measurements again allowed the identification of distinct groups of cells (using k-means clustering) that corresponded to cells that differ in their number of *ori* (Figure S1E). We used this information to determine the average number of origins (<*ori*>) and extract the relative duration of the C+D period (Figure S1E).

The above-described methodology could not be used for the parent strain in the 5 richest conditions (LB, TSB, PYE, NB, and BHI), in which timings for DNA replication (because of the presence of more than two overlapping rounds of DNA replication) or nucleoid constriction (because it occurred in the previous generation) could not be reliably extracted.

Extraction of cell sizes at different cell cycle events

Assuming that individual cells grow exponentially at the single-cell level (in terms of cell or nucleoid length, area, volume, and surface area), the cell size at different cell cycle events was calculated based on the relative timing of a cell cycle event and the average cell size, as described previously.[20]

Reproducibility and effect of kanamycin

To verify the reproducibility of our experiments and assess the potential effect of the presence of kanamycin in the growth media, we imaged the original gene deletion mutants selected from the Keio collection (i.e., prior to phage transduction of the gene deletion into the parent strain expressing the FtsZ-Venus^{SW} and SeqA-mCherry markers) in M9gly with and without kanamycin (50 μg/ml). As before,[35] we found a strong correlation between cell length and width across duplicates, indicating good reproducibility (Figure S1G). For cell length, the presence of kanamycin led to a slight but consistent increase in cell length (Figure S1G). Therefore, for our study, we opted to grow and image the 806 deletions strains carrying both FtsZ-Venus^{SW} and SeqA-mCherry markers without kanamycin in the different growth media. Since the kanamycin resistance marker (which marks the gene deletion of each strain) is chromosomally encoded and is inserted in a gene for which the coding sequence is largely deleted,[109] we do not anticipate that the absence of kanamycin in the growth medium will have any detrimental effect to data interpretation.

Growth rate measurements

Growth rates were extracted from growth curves after well-specific blanking.[119] Blank values were obtained by averaging the first three optical density measurements of an experiment (during which cultures had not yet reached the detectable range of the microplate reader). The maximal growth rate was extracted from the corrected growth curves by fitting the Gompertz function.[120] To account for plate-to-plate variability, we set the median growth rate values for each plate in a given nutrient condition to the median growth rate value of the parental strain in that same nutrient condition.

Normalized score calculations

For each population-level feature in one of the four nutrient conditions in which we sampled our gene deletion mutant library, we also calculated normalized scores (*s*):

$$s = 1.35 \times (F_i - \text{median}(F_{i^{parent}})) / \text{iqr}(F_{i^{parent}})$$

where F_i is the measured value of feature *i* in a nutrient condition, F_i^{parent} are the values of the parent strain for that feature in the same nutrient condition and iqr is the interquartile range. We used this calculation based on the median and the interquartile range as it is

more robust to outliers (compared to a typical z-score calculation). Given that the interquartile range of normally distributed data is equal to 1.35 times their standard deviation, we scaled the score by this factor to express the scores in terms of standard deviations away from the median of the parent values.

Demographs

Demographs, which are linear representations of integrated fluorescence of cells sorted by their length,[60] provide an overview of fluorescence signal dynamics from cell birth to division. Demographs in Figure 3C were constructed using the MATLAB function normLDemographOriented.m. Demographs in Figure 5H were constructed within Oufti.

Correlation coefficients

Spearman correlation coefficients (ρ) between variables were calculated using MATLAB's built-in corr function.

Unconstrained linear fits

Unconstrained linear fits were performed using MATLAB's built-in polyfit function.

K-means clustering

K-means clustering was performed sing MATLAB's built-in kmeans function.

False discovery rate calculation

The expected false discovery rate of incorrectly identifying a deletion strain as one with a deviating phenotype ($|s| > 3$) for a single feature in at least 1 nutrient condition was calculated using the binomial formula ($P(x) = \frac{n!}{(n-x)!x!}p^x q^{n-x}$).